# CRUSTAL STRUCTURE OF THE ALASKA SUBDUCTION ZONE ACROSS THE 2021 M8.2 CHIGNIK EARTHQUAKE RUPTURE AREA FROM WIDE-ANGLE SEISMIC DATA

By Joshua A. Burstein

A Thesis
Submitted in Partial Fulfillment
of the Requirements for the Degree of
Master of Science
in Geology

Northern Arizona University
August 2023

Approved:
Donna Shillington, Ph.D., Chair
Ryan Porter, Ph.D.
Christine Regalla, Ph.D.
James Gaherty, Ph.D.

# ABSTRACT

# CRUSTAL STRUCTURE OF THE ALASKA SUBDUCTION ZONE ACROSS THE 2021 M8.2 CHIGNIK EARTHQUAKE RUPTURE AREA FROM WIDE-ANGLE SEISMIC DATA

JOSHUA A. BURSTEIN

Understanding the influence of large-scale crustal structure on megathrust slip behavior is essential for evaluating seismic and tsunami hazards at convergent plate margins. The subduction zone offshore of the Alaskan Peninsula is an excellent area to examine controls on subduction zone behavior because it has experienced a sequence of recent large earthquakes and it exhibits dramatic along-strike variability in seismicity and geodetic locking. The incoming sediments and oceanic plate in this region have been cited as factors controlling variability in megathrust slip behavior, but the influence of the overriding continental plate is less well studied. Here we focus on the Semidi segment of the Alaska subduction zone, which is strongly locked and regularly ruptures in great (M>8) megathrust earthquakes, including the July 2021 M8.2 Chignik earthquake. We present a two-dimensional P-wave seismic velocity model along a ~365-km-long profile obtained by joint reflection-refraction tomographic inversion of wide-angle seismic (WAS) data collected in 2011 aboard the R/V *Marcus G. Langseth*. Model uncertainty was estimated using a Monte Carlo approach. The resulting P-wave velocity model displays large-scale velocity variations in the overriding plate that constrain the extent of the accretionary prism and accreted crustal terranes that form the overriding plate: the Prince William and Chugach terranes. Shallow slow slip and afterslip are focused beneath the accretionary prism and younger, lower velocity Prince William Terrane while rupture in the 2021 earthquake is concentrated below the higher velocity Chugach terrane, suggesting that the upper plate influences slip behavior here.

# ACKNOWLEDGEMENTS

Throughout my time at Northern Arizona University and the duration of this project, I have received so much support and kindness. I want to express my deepest gratitude to all the friends and great humans that I had the pleasure of interacting with at NAU and the greater Flagstaff community.

Firstly, I would like to thank my graduate advisor, Dr. Donna Shillington. Thank you very much for this opportunity and the pleasure of working with you. The completion of this project would not have been possible without your extraordinary expertise, guidance, and mentorship. I would also like to thank my committee members: Dr. Christine Regalla, Dr. James Gaherty, and Dr. Ryan Porter. Your feedback and expertise have been invaluable to both this project and to furthering my knowledge and interest in the earth sciences.

I would also like to thank my fellow graduate students within the School of Earth and Sustainability and my colleagues within the NAU Tectonics and Geophysics Group. Lastly, I would like to thank my family, Yo, Dan, Sam, and Jake Burstein, for their unwavering support of me through the last few years.

# Table of Contents

# List of Tables

# List of Figures

## 1. Introduction

Subduction zones produce the largest and most devastating natural disasters including large earthquakes, tsunami, landslides, and volcanic eruptions (Hilley et al., 2022). Therefore, it is of the upmost importance to understand the physical controls on subduction zone processes in order to properly assess hazards for these settings. The overarching motivation for this study is to evaluate the physical properties that control fault slip on subduction zone megathrust faults.

Subduction zone megathrust faults exhibit depth-varying rupture behavior. The shallowest portion of the megathrust, from the trench down to ~10 km depth below sea level, is generally under relatively low confining pressure and generally undergoes aseismic slip or stable sliding (Lay et al., 2012). However, in some circumstances, this region can experience large coseismic slip that ruptures all the way to the trench generating a tsunami. Earthquakes generated in this region possess characteristic low rupture speeds and are deficient in high frequency energy (Lay et al., 2012; Sallarès & Ranero, 2019). The central region of the megathrust (~10-30 km depth) hosts the largest amount of geodetic locking and generally the largest amount of earthquake slip (Lay et al., 2012; Scholz, 1998). Farther downdip (~30 – 55 km depth), the megathrust is thought to host smaller asperities surrounded by conditionally stable regions that can also experience slow slip and other transient behaviors. Finally, at depths >~55 km the megathrust exhibits low-frequency earthquakes, seismic tremor, and slow slip events as the megathrust transitions to stable sliding or ductile deformation below the seismogenic zone (Lay et al., 2012).

A number of interrelated factors have been offered to explain the diversity in subduction zone earthquake behavior, such as pore fluid pressure and/or heterogeneity along the plate interface, rigidity of the overriding plate, and temperature structure (Li et al., 2018; Saffer &

Tobin, 2011; Sallarès & Ranero, 2019; Shillington et al., 2022; Wang & Bilek, 2014). In one classic model of subduction zone megathrust behavior, the downdip limit of the seismogenic zone corresponds to the depth on the megathrust where temperatures reach ~ 350 - 450°C, or where the subducting plate boundary intersects the overriding plate's fore-arc mantle (Oleskevich et al., 1999). Where fore-arc mantle overlies the plate boundary, hydrated minerals such as talc and serpentine are thought to be present and are hypothesized to control frictional properties along the plate interface. The thickness, state of stress, rigidity, and permeability of the overriding plate could also influence earthquake behavior and/or the distribution of fluids along the plate boundary (Audet et al., 2009; Bassett et al., 2016; Sallarès & Ranero, 2019; L. M. Wallace et al., 2012). For example, interseismic locking and slip during the 2011 Tohoku-oki earthquake are focused beneath a terrane in the overriding plate that is denser and more rigid terrane than neighboring terranes (Bassett et al., 2016; Kimura et al., 2022). The state of stress (compressional vs. extensional stress) and composition of accreted terranes in the overriding plate have also been proposed to influence the permeability and pore fluid pressure of the overriding plate and along the plate boundary megathrust (Audet et al., 2009; L. M. Wallace et al., 2012). In the Hikurangi margin in New Zealand, the state of stress in the overriding plate has been reported to influence the strength of interseismic coupling along the plate boundary and the depth of slow-slip events (SSEs) (L. M. Wallace et al., 2012). Here we evaluate the role of the upper plate in influencing megathrust slip behavior in the Alaska subduction zone by constraining upper plate velocity structure using wide-angle seismic data.

## 2. Tectonic and Geologic background

The Alaska subduction zone accommodates the relative motion between two converging tectonic plates: the subducting Pacific plate and the overriding North American plate. The rate of convergence between the two tectonic plates ranges from 51 to 75 mm/yr, with the Semidi segment exhibiting a convergence rate of 60 mm/yr with a generally normal (orthogonal) convergence vector (DeMets et al., 2010; Fig. 1). The Alaska subduction zone exhibits along-strike and downdip variability in present-day geodetic locking, earthquake history and seismicity. Geodetic studies indicate a decrease in plate boundary megathrust coupling from east to west across this region of the Alaska subduction zone (Fig. 1). The Semidi segment, the focus of this study, exhibits strong coupling (locking fraction of ~0.8) in the eastern portion to moderate coupling (locking fraction of ~0.4 ) in the western portion (Drooff & Freymueller, 2021; Elliott et al., 2022; Li & Freymueller, 2018; Xiao et al., 2021).

The Semidi segment also hosts great (M>8) earthquakes about every 50-75 years (Davies et al., 1981). The two most recent great earthquakes to have occurred within the Semidi segment are the 1938 M8.3 earthquake and the 29 July 2021 M8.2 Chignik earthquake. There are no coseismic slip models available for the 1938 event, however the rupture zone for this event is estimated to be approximately 300 km margin-parallel based on relocated aftershocks (Davies et al., 1981; Sykes, 1971; Tape & Lomax, 2022; Fig. 1). The 1938 event generated a modest tsunami and is estimated to have released more seismic moment in the eastern portion of the rupture zone than the west (Johnson & Satake, 1994). Although most studies based on aftershocks, teleseismic data and tsunami measurements estimate that the 1938 earthquake was confined to the deep portion of the megathrust (Davies et al., 1981; Estabrook et al., 1994; Johnson & Satake, 1994; Tape & Lomax, 2022), a recent study based on local tide gauge data suggests that rupture was shallower and farther east than originally proposed (Freymueller et al., 2021).

Rupture models for the 2021 M8.2 Chignik earthquake also indicate rupture of the deep portion of the megathrust (20-40 km depth) with peak slip of 8.6 m near the hypocenter at ~26 km depth (Elliott et al., 2022; Liu et al., 2022; Ye et al., 2022). The 2021 event is estimated to have ruptured the western two thirds of the 1938 rupture zone (Liu et al., 2022; Ye et al., 2022). Although the July 2021 event was speculated to have potentially  loaded the shallow megathrust (<20 km depth) (Elliott et al., 2022), a recent seafloor geodetic study has reported approximately 2-3 meters of shallow (<10 km depth) megathrust afterslip within ~2.5 months after the 2021 event, which may decrease the possibility of a shallow earthquake rupture (Brooks et al., 2023). Likewise, a recent seafloor geodetic study reported a slow-slip event (SSE) occurred on the shallow megathrust in the Semidi segment in 2018, up-dip of and preceding the 2021 event (He et al., 2023). Thus, the shallower portion of the megathrust could experience both earthquake slip and slow slip (He et al., 2023).

While the moderately coupled Semidi segment regularly ruptures in great (M>8) earthquakes every 50-75 years, it exhibits low levels of <M8 earthquakes (Davies et al., 1981; Shillington et al., 2015). Conversely, the neighboring weakly-coupled Shumagin Gap last hosted a great earthquake about 150 years ago, exhibits high levels of <M8 earthquakes, and regularly ruptures in M7.x earthquakes, most recently in the 2020 Mw7.8 Simeonof earthquake (e.g., Liu et al., 2020, Xiao et al., 2021).

Previous work showed that variations in the characteristics of the incoming oceanic Pacific plate could contribute to the along-strike differences in earthquake behavior between these two neighboring segments of the Alaska subduction zone (Von Huene et al., 2012; Li et al., 2018; Shillington et al., 2015; Wei et al., 2021). Shillington et al. (2015) observed along-strike variations in bending faulting and hydration of the incoming plate with less bending faulting and hydration in the Semidi segment. The incoming plate of the Semidi segment is characterized by a relatively thick (~1-1.5 km) sequence of sediments (Li et al., 2018), including an ~800-m-thick layer of distal turbidites from the Eocene-age Zodiac Fan, a pelagic sediment layer, and trench fill associated with glacial erosion debris supplied by the still active Chugach-St. Elias orogeny (Von Huene et al., 2012; Stevenson et al., 1983; Fig. 1). Part of this sedimentary section subducts with the downgoing plate, forming a relatively continuous 600-m-thick sediment layer along the plate interface that is characterized by low seismic velocities and elevated pore fluid pressures (Li et al., 2018). The relatively thick, continuous, and overpressured sediment layer entering the Semidi segment may form velocity-strengthening material on the shallow plate boundary megathrust and inhibit rupture along the shallow megathrust (Li et al., 2018). However, at greater depths in the seismogenic zone, the sediment layer may act as a large, coherent asperity along the plate interface as the sediment package compacts and dewaters due to increasing temperatures and lithostatic pressures (J. Li et al., 2018; Miller et al., 2021). Together, the thicker sediments and limited bending faulting on the incoming plate imply a relatively smooth, more homogeneous plate interface at depth, and therefore, may form a more uniform region of coupling that favors rupture in large earthquakes. Additionally, Wei et al. (2021) used deep intraplate earthquakes and trace element signatures of lavas from Alaska Peninsula volcanoes to support the idea of continued influence of sediments, faulting, and hydration at depth.

The overriding continental plate may also influence subduction zone processes in the Alaska subduction zone (e.g., Shillington et al., 2022). The overriding continental plate of the Alaska subduction zone is comprised of a series of accreted terranes that young to the south: the Permian to late Mesozoic Peninsular Terrane, the Cretaceous Chugach Terrane, and the Paleocene Prince William Terrane (Horowitz et al., 1989; Figs. 1 and 2). The southernmost and youngest of these accreted terranes is the Paleocene Prince William Terrane, which largely consists of Paleocene and Eocene turbidites, Oligocene, Miocene and Plio-Pleistocene shelf strata, and minor mafic volcanic rocks (Horowitz et al., 1989; Braden & Behr, 2021). To the north is the Cretaceous Chugach Terrane. Onshore geologic exposures from the nearby Kodiak Island and Kenai Peninsula (Fig. 1) show that the Chugach Terrane is largely composed of Triassic to Cretaceous tectonic mélange consisting of deformed oceanic basalts, chert, shale, rare exposures of ultramafic rocks, and a series of deep-water turbidite sequences that reach greenschist metamorphic facies peak pressure and temperature conditions, significantly more metamorphosed and reworked than the exposed rocks of the younger Prince William Terrane to the south (Plafker & Berg, 1994; Braden & Behr, 2021). Separating the Paleocene Prince William Terrane and the Cretaceous Chugach Terrane is a tectonic boundary commonly referred to as the Contact Fault (Horowitz et al., 1989; Plafker & Berg, 1994). Exposures of the Contact Fault on Kodiak Island indicate the Contact Fault has thrust sense of motion and records the ongoing process of accretion and underplating of material provided by the downgoing plate since at least the Cretaceous (Sample & Moore, 1987; Horowitz et al., 1989). Onshore geologic exposures also reveal that the Chugach and Prince William terranes are “stitched” together by Paleocene granitic intrusions (W. K. Wallace & Engebretson, 1984). The northernmost and oldest of the accreted terranes in this region is the Permian to Late Mesozoic Peninsular Terrane. This terrane is mainly comprised of highly metamorphosed greenschist and blueschist facies rocks, metacherts, and volcaniclastic turbidites (Horowitz et al., 1989).

Wide-angle seismic data reveal a landward increase in P-wave velocity in the overriding plate in the Shumagin Gap, implying a landward increase in rigidity (Shillington et al., 2022). Additionally, MCS imaging of the Shumagin Gap (ALEUT Line 5; Fig. 2) revealed a major active normal fault that is likely a reactivated fault that was inherited from the collision between the Prince William and Chugach terranes via the Contact Fault  (Bécel et al., 2017; Shillington et al., 2022; Von Huene et al., 2019). This active normal faulting activity likely suggests the overriding plate is undergoing extensional stress in the weakly coupled Shumagin Gap. Estimates of the rigidity and thickness of the overriding plate in the moderately coupled Semidi segment and their relationship to plate boundary properties and megathrust slip history are not yet known and that is the aim of this study.

## 3. Wide-angle Seismic Data Acquisition, Processing, and Analysis

### 3.1 Data Acquisition

In 2011, the Alaska Langseth Experiment to Understand the megaThrust (ALEUT) acquired 3700 km of multichannel seismic (MCS) reflection and 800 km of wide-angle seismic (WAS) data across the Alaska subduction zone collected with ocean bottom seismometers (OBS) (Fig. 2). Here we focus on wide-angle seismic profile ALEUT Line 3 acquired on a ~365-km-long profile across the central portion of the Semidi Segment, which comprises 21 OBS at an average spacing of ~15.8 km (Table 1; Figs. 2, 3). The wide-angle seismic refraction data were acquired using four-component OBS recorded at 200 Hz from the Scripps Institute of Oceanography (SIO). The SIO four-component OBS include a L28 gimbaled three-component geophone and a hydrophone component. The source of seismic energy was the 6,600 cu. in. tuned 36-element airgun array of the R/V *Marcus G. Langseth*. The airgun array was towed at 12 m depth. The shot interval was 310 m (~120 s) for all OBS shooting. All OBS instruments were recovered, and all instruments recorded high-quality wide-angle seismic data except for OBS 314, which had timing issues, and we do not include in our analysis.

### 3.2 OBS data processing

Simple processing steps were applied to WAS data to relocate the OBS and remove noise to facilitate identification and picking of the travel-times of first-arrival refractions and secondary-arrival reflections. OBS were relocated by picking water wave arrivals and using a grid search to determine the best fitting position including constraints on water velocity and bathymetry. All other data processing steps were performed using the open-source seismic processing software Seismic Un*x (Cohen & Stockwell, 2004). The processing sequence included a minimum-phase Butterworth, trapezoidal bandpass filter with pass corners of 3-5-15-20 Hz and an offset-dependent gain. The minimum-phase bandpass filter ensured an increase in signal to noise ratio without altering or shifting the original signal, and the offset-dependent gain amplifies coherent signals at longer offsets (Fig. 4). A reduction velocity of 8 km/s was applied to view seismic phases more easily at long offsets and assess their apparent velocities. In a reduced travel-time seismogram, a seismic phase travelling with an apparent velocity of 8 km/s will appear horizontal (e.g., Fig 4).

### 3.3 Seismic phase picking and uncertainties

We used OpendTect to pick both first arrivals and secondary arrivals to use for tomographic inversions. Previous studies had performed tomographic inversions of the OBS instruments that overly the incoming plate of the Semidi segment: OBS 301 – 306 (Shillington et al., 2015). For this study we aimed to constrain the velocity structure of the overriding plate in the Semidi segment. Thus, we focused our efforts on the OBS instruments that overly the overriding plate spanning from the trench to the most landward (northwestward) portion of the ALEUT Line 3 profile: OBS 307 – 321 (Figs. 2, 3). Overall, the OBS data displays clear first arrivals at offsets up to 100-125 km. Data quality for different seismic phases varied with offset, variations in the complexity of geology along the profile, and between individual instruments. Travel-time picks were made on the hydrophone component of all instruments due to high data quality relative to the three-component geophone. Upon visual inspection, uncertainties were assigned to seismic phases that ranged from 50 ms for the clearest first arrivals and 100 ms for secondary arrivals (Table 2).

In order to quality-control travel-time picks and assess the consistency of phase identification between different instruments, we employed reciprocity checks (Fig. 5). For source-receiver pairs that are reciprocal, the corresponding travel-times of any seismic phase arrival should be the same regardless of Earth structure (Zelt, 1999) after correcting for water-depth differences between OBS.

For the instruments that overlie the overriding pate near the trench (OBS 307-311), we identified first arrivals at close offsets (0.5-10 km offset) that displayed relatively slow apparent velocities. We interpreted these arrivals as rays refracting through sediments associated with trench-fill and the accretionary prism (*Psed*). At offsets of ~10-40 km, we observed a phase with higher apparent velocities that we interpreted as refractions through the continental crust (*Pg_short*). The apparent velocities and offset range of these arrivals varied considerably with distance from the trench due to the complex bathymetry and structures in the forearc and thickening crust of the overriding plate. At offsets of ~10-50 km, we observed a bright secondary arrival for these trenchward OBS that we interpreted be reflections off of the top of plate boundary (*PpbP*). Due to the complex geometry of the subduction zone near the trench, instruments in this area yielded seismograms that display complicated interactions between secondary arrivals and arrivals associated with multiple energy. In order to distinguish between these two coincident arrivals, we utilized reciprocity checks (Fig. 5).

Seismograms of instruments that overlie the landward part of Line 3 (OBS 312-321) contained continental crustal refractions at offsets of ~0.5-100 km, which we refer to as *Pg_short*. On OBS 315-318 and OBS 320-321, we observed crustal refraction arrivals at longer offsets that varied between OBS, but were generally at ~50-125 km offset. Due to the pervasiveness of strong reverberations at large offsets in these landward OBS seismograms, we assigned a larger picking uncertainty to these travel-time picks and refer to these picks as *Pg_long*. It is important to note that both Pg_short and Pg_long are interpreted to be continental crustal refractions and the only difference between the two phases are the assigned picking uncertainty (see Table 2). On most of these OBS, a bright secondary arrival was observed at offsets of ~60-100 km, however this varied between different OBS overlying the overriding plate. We interpreted this reflection phase as arising from the top of the plate boundary. Interpretation of instruments in shallow water was complicated by reverberations, making identification of secondary arrivals difficult. Again, we utilized reciprocity checks to determine the geometry of secondary arrivals in this region and interpreted these to be reflections off of the top of the plate boundary. We did not observe reflections off the base of the continental crust landward of its divergence from the plate boundary.

## 4. Velocity Modelling

We performed a 2-D tomographic inversion of the WAS travel-time data using Tomo2D, a joint reflection/refraction inversion code (Korenaga et al., 2000). The inversion code utilizes a starting 2-D velocity model and travel-time picks for iterative ray tracing and inversion for a perturbed velocity model and depth to a floating reflector. The model is parameterized as a sheared mesh hung from the sea-surface. We utilized a fixed grid spacing, with a vertical node spacing of 0.2 km and horizontal node spacing of 1 km. The model space spans 366 km in the x-direction and 50 km in the z-direction for a total of 366 x 251 = 91866 model nodes.

To calculate the forward problem, Tomo2D employs a hybrid ray-tracing approach based on the graph and ray-bending refinement methods (Korenaga et al., 2000). The inversion step utilizes a sparse matrix solver LSQR to output a damped, weighted least-squares solution (Korenaga et al., 2000). Model parameters output from the inversion code include P-wave velocity at each model node and a depth to a floating reflector.

The inverse problem posed by this tomographic inversion was largely underdetermined, and regularization was needed to stabilize the inversion. This was achieved through smoothing constraints on both velocity and floating reflector depth. We implemented a set of vertically and horizontally variable correlation lengths that define the magnitude of smoothing allowed between each model node in each direction. Overall smoothing parameters for velocity (Sv) and reflector depth (Sd) were also used to control the inversion's weighting of smoothing constraints with respect to data fit. A weighting parameter *w* was also implemented to weight the importance of perturbations in velocity versus floating reflector depth.

Similar to Korenaga et al. (2000), we employed an iterative approach, using the output of model parameters of the previous iteration as the input for the subsequent iteration. At each inversion stage, the smoothing parameter Sv was gradually decreased between iterative steps until the root mean square (RMS) misfit value of modelled travel-times equaled approximately the uncertainty assigned to the observed travel-time picks, or similarly, when the chi-squared misfit value equaled ~1. Inversion statistics are provided in Table 3. In order to preserve the resolved structures within each model layer, we followed a layer-stripping / top-down modelling approach (e.g., Horning et al., 2016; Korenaga et al., 2000). As we began the inversion, we wanted to ensure that velocity perturbations to the starting model only occurred within a defined model layer which is constrained by a defined seismic phase. This was performed by implementing large damping values above the target model layer. As we progressed to deeper layers, we held the structure above fixed and reset the starting model for the target layer. This process ensured that velocity perturbations only occurred within a defined layer of the model at each step within the inversion.

### 4.1. Overriding Plate model

Here, we summarize the inversion steps employed to create a seismic velocity model of the overriding continental plate along profile ALEUT Line 3. This model consists of a total of 6522 travel-time picks observed on 14 OBS (307-321) spanning the trench to the most landward seismic shot. As described above, we followed a top-down modelling approach in which we inverted the shallowest layers first before progressing to deeper model layers.

#### 4.1.1. Overriding Plate Stage 1: Sediments

We refer to “sedimentary refractions” as any first-arrival of seismic energy that displays a relatively slow apparent velocity (<~4 km/s) at relatively small source-receiver offsets (generally 0.5-10 km offset) to the respective OBS. We only identified this specific seismic phase on four OBS (307-311), which overly the trench and accretionary prism, for a total of 131 travel-time picks. We interpreted these arrivals as refractions through shallow material associated with trench-fill sediments and the accretionary prism, which we call *Psed* (Table 2). Since we parametrized our velocity model as a mesh hung from the sea-surface, we set large damping values (1000) within the water column above the seafloor and only allowed the velocities below the seafloor to vary. Seafloor depths were extracted from multibeam bathymetry collected by the

*R/V Langseth's* EM122 echosounder. Water column velocities were set to a constant P-wave velocity of 1.5 km/s. Horizontal correlation lengths increased from 5 km at 0 km depth to 15 km at 50 km depth. Vertical correlation lengths increased from 0.25 km at 0 km depth to 2 km at 50 km depth. After inverting these *Psed* arrivals, we achieved convergence within 8 steps, with 5 iterations within each step, by decreasing the overall velocity-smoothing (Sv) parameter between each iterative step.

### 4.1.2. Overriding Plate Stage 2: Crustal refractions

The "final" model of Stage 1 was then used as the starting model for Stage 2, in which we brought a total of 4824 continental crustal refraction travel-time picks into the inversion (Pg_short and Pg_long). To ensure that only continental crustal velocities were perturbed in the inversion, we defined high damping values above the basement. The basement depth was extracted from coincident MCS data (Kuehn, 2019). Horizontal correlation lengths increased from 5 km at 0 km depth to 15 km at 50 km depth, and vertical correlation lengths increased from 0.25 km at 0 km depth to 2 km at 50 km depth. After inverting both continental crustal refraction phases, we achieved convergence within 5 steps, each with 5 iterations, by decreasing the overall velocity-smoothing (Sv) parameter between each iterative step.

### 4.1.3. Overriding Plate Stage 3: Plate boundary reflections

In Stage 3, we used the "final" model from Stage 2 as the starting model to begin inverting plate boundary reflections (PpbP). Here, we imposed the same damping values as Stage 2 in which all model parameters above the MCS-derived basement were kept constant and we only allowed for the model parameters below the basement horizon to perturb. After inverting a total of 1567 plate boundary reflection travel-time picks, we achieved convergence within a reasonable misfit within 7 steps, each with 5 iterations, again decreasing the overall velocity-smoothing (Sv) parameter between each iterative step.

### 4.2 Monte Carlo uncertainty analysis

To create a final P-wave velocity model and quantify model parameter uncertainty, we employed a Monte Carlo approach using tomographic inversion code Tomo2D (Korenaga et al., 2000). Following the layer-stripping strategy described in the previous section, we performed 100 inversions for each layer, varying the starting model velocities, the initial floating reflector geometry, and applying random perturbations to the travel-time picks. The magnitude of random perturbations to the travel-time picks was weighted by the individual phase's picking uncertainty. The average of these models is the final model, and the standard deviation of these models provided an estimation of model uncertainty. The final model of the overriding plate has an overall a chi-square misfit of 1.50 and RMS misfit of 57 ms (Table 3, Fig. 6). The sedimentary and continental crustal velocities generally have standard deviations of less than 0.1 km/s down to ~25 km depth. There was greater uncertainty for the lower crustal velocities and plate boundary depth from ~30-40 km depth. This was due to the fact that this portion of the model was only constrained by wide-angle reflections, and there is thus trade-off between velocity and depth to the plate boundary megathrust. The thickness of the red line on the plate boundary in panel B indicates the uncertainty of plate boundary depth (Fig. 6).

## 5. Results

The final Line 3 velocity model constrains the large-scale P-wave seismic velocity structure of the overriding plate in the central Semidi Segment. In general, velocities in the overriding plate increase landward, with prominent increases in Vp at model distance 160 km (note abrupt shallowing on 4 and 5 km/s contours, Figs. 6, 7) and at model distances 220-230 km (note abrupt shallowing on 5 and 6 km/s contours, Figs. 6, 7). We interpret both prominent increases in Vp to indicate changes in lithology between geologic domains in the overriding plate in the Semidi segment.

Near the trench (model distance ~120 – 220 km), we observe a package of material with a relatively low Vp ranging from 2 - 4.5 km/s down to about 10 km depth. We interpret this portion of the model as a combination of accreted sediments from the incoming plate and trench fill associated with glacial erosion debris supplied by the still active Chugach-St. Elias orogeny (Von Huene et al., 2012; Stevenson et al., 1983). We also observe a marked jump in Vp to 5 km/s near model distance 160 km (~45 km from the trench) that we propose to indicate a transition from the accretionary prism complex to a more rigid material in the continental crust; hereafter, we refer to this transition as the backstop.

Between model distances ~160 – 220 km we observe crustal velocities between 5-6.2 km/s, consistent with very low-grade (up to prehnite-pumpellyite facies) metamorphosed sediments and/or granitic intrusions (Christensen & Mooney, 1995). We interpret this portion of the model to be correlated to the Paleocene Prince William Terrane, which consists of Paleocene and Eocene turbidites and minor mafic volcanic rocks, and Paleocene granitic intrusions according to onshore geologic exposures of this terrane on Kodiak Island and Kenai Peninsula (Horowitz et al., 1989; Braden & Behr, 2021).

Near model distance 220 km (~100 km from the trench), we observe another prominent increase in Vp (note abrupt shallowing on 5 and 6 km/s contours, Figs. 6, 7). This increase approximately corresponds to a previously estimated boundary between the Paleocene-age Prince William Terrane in the south and the Cretaceous-age Chugach Terrane to the north, commonly referred to as the Contact Fault (Horowitz et al., 1989; Plafker & Berg, 1994; Figs. 1, 2). Onshore geologic exposures from Kodiak Island and Kenai Peninsula show that the Chugach Terrane is largely composed of Triassic to Cretaceous tectonic mélange consisting of deformed oceanic basalts, chert, shale, rare exposures of ultramafic rocks, Paleocene granitic intrusions, and a series of deep-water turbidite sequences that reach greenschist metamorphic facies peak pressure and temperature conditions. Rocks of the Chugach Terrane are significantly more metamorphosed and reworked than rocks found in the younger Prince William Terrane to the south (Plafker & Berg 1994; Braden and Behr, 2021).

Between model distances 220-320 km, the Line 3 velocity model displays velocities ranging from 5-6.8 km/s (Figs. 6, 7); these observed crustal velocities are consistent with more metamorphosed metasediment sequences, mafic units, and Paleocene granitic plutons within the Chugach Terrane, resulting in a bulk increase in P-wave velocities in this region of the overriding plate (Christensen & Mooney, 1995). We interpret the prominent increase in velocity at model distance 220 km to be a suture zone between the Prince William and Chugach terranes, where the velocity jump is the result of thrusting of more highly metamorphosed and mafic material of the older Chugach Terrane over the younger, less metamorphosed material of the Prince William Terrane.

The depth and geometry of the subducting plate boundary megathrust is constrained solely by wide-angle reflections from OBS data. On average, our resolved plate interface displays an average dip of about 10º. Due to limited ray coverage resulting from the experiment geometry and noisy reverberations within the most landward OBS, we are not able to constrain the geometry of the plate interface deeper than approximately 40 km depth and farther landwards than model distance 260 km (~140 km from the trench). Further work can be done to include any land-based seismometers located onshore (farther landwards than the Line 3 profile) that might constrain the depth and geometry of the continental Moho and its intersection with the subducting plate boundary megathrust (e.g., Shillington et al., 2022). The plate boundary megathrust resolved in our Line 3 velocity model is consistently steeper and deeper than that modelled by a seismicity-based subduction zone plate interface model, Slab 2.0 (Hayes et al., 2018). Our new result is in agreement with other studies that used teleseismic earthquake waveforms and GPS data to constrain the 2021 rupture area and found a preferred slab geometry that is also steeper and deeper than Slab 2.0 (e.g., Liu et al., 2022) and with coincident reflection imaging using a simplified velocity model (Kuehn, 2019).

## 6. Discussion

The Line 3 final velocity model based on OBS data can be used to constrain the structure of the overriding plate and geometry of the megathrust. Here we integrate the new P-wave velocity model with coincident seismic reflection imaging and information on upper plate terranes from onshore geology to examine the possible contribution of large-scale velocity variations to megathrust behavior in this region. Recent great earthquakes in the Semidi segment of the Alaska subduction (1938 Mw8.2 earthquake and the 2021 Mw8.2 Chignik earthquake) appear to have ruptured the plate boundary at depths >20 km (Davies et al., 1981; Elliot et al., 2022; Liu et al., 2022; Mulia et al., 2022; Ye et al., 2022; Fig. 1). At shallower depths, recent seafloor geodetic studies have reported aseismic slip along the shallow portion of the megathrust both preceding the 2021 earthquake (He et al., 2023) and following the 2021 earthquake (Brooks et al., 2023) (Fig. 1). However, seismic slip is also inferred to have occurred on the shallow plate boundary based on tsunamigenic events in the historical record (e.g., 1788; Davies et al., 1981). Thus, this part of the plate boundary may be capable of both seismic slip and slow slip. We evaluate the possible influences of overriding plate structure on these patterns of slip in the Semidi segment and then compare with the creeping Shumagin Gap to the west.

## 6.1: Influence of upper plate structure on megathrust slip in the Semidi Segment

### *6.1.1: Accretionary prism*

The new Line 3 velocity model constrains the width and thickness of the modern accretionary prism in the central Semidi segment. Based on our model, our interpreted accretionary prism spans from model distances 115-160 km (approximately 45 km from the trench) and extends to about 10 km depth. The accretionary prism in the central Semidi segment is significantly wider than in the Shumagin Gap (e.g., Li et al., 2018; Fig. 10). We attribute this pattern to an increase in sediment thickness on the incoming plate supplied by the Eocene-age Zodiac fan and glacial debris provided by glacial erosion of the Chugach-St. Elias orogeny that was transported to the southwest along the continental shelf (Stevenson et al., 1983; Von Huene et al., 2012). Coincident MCS data show that the upper part of the incoming sediment section (trench fill and pelagic sediment on the Pacific plate) is accreted and deformed by thrust faulting and folding within the accretionary prism, while most of the older Zodiac fan subducts (Li et al., 2018; Fig. 8). The subducted sediments form a continuous 600-m-thick sediment layer below the accretionary prism characterized by low seismic velocities interpreted to represent elevated pore fluid pressures (Li et al., 2018).

At model distance 160 km, we observe a marked increase in upper crustal seismic velocity, which we interpret to mark the landward extent of the accretionary prism and a transition to a presumably more rigid upper plate material, the Prince William Terrane (Figs. 7, 8). Previous seismic reflection studies in the Semidi segment identified a series of landward dipping reflections that they interpreted as the backstop fault zone (BSFZ) (e.g., Von Huene et al., 2016, 2021); the interpreted BSFZ is located about 30-45 km from the trench, near the location of our proposed transition from the accretionary prism complex to the Prince William Terrane. Additionally, coincident MCS data along Line 3 display moderately large-amplitude landward-dipping reflectors in this same region (Fig. 8; Li et al., 2018; Kuehn, 2019). We also observe a high at the seafloor associated with the surface expression of this fault zone and a change in seafloor dip (Fig. 8). Combined, these observations suggest that there is an active out-of-sequence fault located ~45 km from the trench that separates more compliant material within the actively deforming accretionary prism from more rigid Prince William Terrane rocks.

Seafloor vents have also been observed within the forearc region of the eastern Semidi segment in acoustic backscatter images of the seafloor in the same region as our proposed backstop between the accretionary prism and the Prince William Terrane and possible out-of-sequence faults imaged in MCS data (model distance 160 km; Von Huene et al., 2021; Krabbenhoeft et al., 2021) (Figs. 1, 8). These forearc seafloor vents are similar to ones well studied along the Middle America margin in which heat flow probes and fluid chemistry indicates fluid sources at or near the plate boundary interface (Von Huene et al., 2021; Ranero et al., 2008; Sahling et al., 2008). We propose the landward dipping structures observed in coincident MCS images (Fig. 8) near the interpreted landward extent of the accretionary prism based on the Line 3 velocity model could be providing pathways for the fluids to migrate from the plate boundary to the seafloor in the form of seafloor vents and/or seeps. More near-bottom surveying must be conducted in order to corroborate this hypothesis.

Taken together, the constraints described above suggest that the megathrust within ~45 km of the trench lies within a 600-m-thick low-velocity zone interpreted to represent an overpressured subducted sediment layer and is overlain by an accretionary prism. As a result, this part of the megathrust may predominantly experience shallow slow slip or stable sliding. This is consistent with the absence of shallow megathrust rupture during the recent 1938 and 2021 megathrust earthquakes in this segment based on aftershock distribution, teleseismic data and tsunami data. However, this part of the plate boundary may experience infrequent great earthquakes as suggested to have occurred in 1788 (Davies et al., 1981). Thus, the slip behavior along the shallow portion of the Alaska megathrust may be similar to the sediment-rich Nankai subduction zone, which experiences shallow slow slip and infrequence earthquake slip (Araki et al., 2017; Fulton & Harris, 2012). New seafloor geodetic data cannot constrain slip and locking at depths <10 km offshore Alaska (Brooks et al., 2023), so further data are needed in order to constrain the slip behavior of the shallowest parts of the megathrust.

### *6.1.2: Accreted crustal terranes in the overriding plate*

The Line 3 velocity model constrains the crustal velocity structure of the overriding plate of the Semidi segment. In general, we observe a landward increase in Vp within the overriding plate, including prominent Vp increases at model distance 160 km, as discussed above, and at model distances 220-230 km (Fig. 7). We interpret the latter to indicate a major structural and lithological boundary between two distinct geologic domains in the overriding plate: the Paleocene Prince William Terrane (model distance 160 – 220 km) and the Cretaceous Chugach Terrane (model distance 220 – 320 km) (Fig. 7). A major tectonic, landward-dipping thrust-sense boundary, known as the Contact Fault, separates the Prince William and Chugach Terranes (Horowitz et al., 1989; Plafker & Berg, 1994; Figs. 1, 2). The estimated location of this boundary within the Semidi segment, based on the westward extrapolation of geologic exposures on

Kodiak Island (Horowitz et al., 1989), approximately corresponds to the marked northwestward increase in Vp observed between model distances 220-230 km within the Line 3 velocity model (Fig 7). Within coincident MCS data along Line 3, we do not observe a clear seismic reflector originating from this proposed suture zone between the overriding plate terranes, so its dip is not constrained here. Our preferred geometry of the Contact Fault within the Line 3 velocity model follows a dip of ~30º, consistent with expected fault geometry for a thrust-sense fault based on Andersonian theory and similar to the geometry of the interpreted reactivated Contact Fault imaged within ALEUT Line 5 (~27º) (Bécel et al., 2017; Shillington et al., 2022).

In comparison with coincident MCS data along ALEUT Line 3, we also observe prominent lower crustal reflections within the Chugach Terrane (model distance ~260 km; Fig. 8). These lower crustal reflections are approximately collocated with an increase in Vp in the lower crust (6.25-6.8 km/s) (Figs. 8, 9). We speculate that these observations of lower crustal reflections and increase in seismic velocities near model distance ~260 km could be consistent with an increase in magmatic intrusions into the Chugach Terrane and/or an increase in metamorphic grade of the material within the Chugach Terrane. Both lower crustal magmatic intrusions and an increase in metamorphic grade would result in increased seismic velocities (Christensen & Mooney, 1995). Seismic reflectivity is frequently attributed to intrusions, including in the upper plate of the Alaska-Aleutians subduction zone (Calvert & McGeary, 2013). Likewise, seismic reflectivity in collision zones has also been attributed to metamorphic fabrics (Knapp et al., 1998). Finally, Paleocene magmatic intrusions and increased metamorphic grade are both consistent with Chugach Terrane lithologies as observed in onshore geologic exposures (Braden & Behr, 2021; Horowitz et al., 1989). It is possible that there are also similar lower crustal seismic reflections indicative of magmatic intrusions present within the Prince

William Terrane, however much of the reflectivity observed within the Prince William Terrane are likely residual multiples of the seafloor (Fig. 9; Kuehn, 2019) and thus are not included in our interpretations/discussions.

One key observation is that most of the earthquake slip that occurred during the 2021 earthquake (Elliott et al., 2022) and possibly the 1938 earthquake (Davies et al., 1981; Tape & Lomax, 2022) seems to have occurred along the deep (>25 km) megathrust overlain by the Chugach Terrane based on our interpreted velocity model (Fig. 8). The region of recently reported aseismic afterslip (Brooks et al., 2023) and slow slip (He et al., 2023) occurred along the shallow (<25 km) megathrust overlain by the Prince William Terrane and possibly the accretionary prism (Fig. 9). The spatial correspondence between variations in recent slip behavior and the Chugach and Prince William terranes implies that the overriding plate could influence megathrust behavior. Here we explore three endmember possibilities in which the upper plate could contribute to the observed earthquake behavior. It is also possible that a combination of these explanations may contribute to behavior, or that the spatial correlation between upper plate properties and slip behavior is a coincidence, and the upper plate exerts no influence on megathrust slip behavior.

A. Variations in permeability of the overriding plate terranes.
B. Large-scale changes in rigidity of the overriding plate terranes.
C. Changes in frictional properties of lithologies bounding the megathrust plate boundary.

*Possibility A:* Differences in permeability between the Prince William and Chugach Terrane could modulate fluid accumulation and the development of overpressures on the megathrust and thus influence seismic behavior. If the lower crustal reflections and increased lower crustal velocities observed between model distances ~260-320 km (Figs. 7, 8, 9) are indeed indicative of either magmatic intrusions or higher metamorphic grade of material within the Chugach Terrane, both propositions could imply that the Chugach Terrane is less permeable than the Prince William Terrane for the following reasons. Extensive magmatic intrusions into the lower crust of the Chugach Terrane could act as an impermeable seal to fluids migrating from the plate boundary and create overpressurized conditions along the deep portion of the plate boundary, similar to observations in Cascadia (Audet et al., 2009). However, based on exposures of the Chugach terrane on Kodiak Island, intrusions are sporadic, thus we consider intrusions unlikely to reduce the bulk permeability of the Chugach terrane. In contrast, the higher metamorphic grade of lower crustal rocks could contribute to lower permeability of the Chugach Terrane compared to the Prince William terrane, due to higher grade rocks having been more compressed and experienced pressure solution that will have collapsed and filled in pores and fractures of the lower crustal rocks.

If the Chugach Terrane is indeed relatively impermeable, this overriding plate terrane could act as a barrier to fluids migrating upwards from the plate boundary, which could either promote accumulation of fluids on the underlying deep (>25 km) megathrust and development of overpressures or channelized flow of fluids updip along the megathrust to shallower depths (Bekins et al., 1994). In the first case, accumulation of fluids on the deep megathrust could lead to development of elevated pore fluid pressures, as suggested in other subduction zones (e.g., Audet et al, 2009), which could reduce effective stress and either promote slow (aseismic) slip or enable seismic slip to deeper depths (Audet et al., 2009; Saffer & Wallace, 2015). The observed relationship between terranes in the overriding plate and recent slip behavior is inconsistent with the hypothesis that elevated pore-fluid pressures promote slow (aseismic) slip along the deep portion of the megathrust. The part of the plate boundary overlain by the less permeable Chugach Terrane recently failed in the 2021 M8.2 Chignik earthquake, while the more permeable Prince William Terrane overlies the part of the plate boundary that has recently experienced slow slip and aseismic afterslip (Fig. 9; Elliott et al., 2022; Liu et al., 2022; Mulia et al., 2022; He et al., 2023; Brooks et al., 2023).

In the second case, the higher metamorphic grade of the Chugach Terrane may act as an impermeable seal that promotes fluids sourced from the deep plate boundary to travel up the plate boundary to lower hydrogeological pressure along the shallow plate boundary. The presence of potential seafloor vents within the eastern portion of the Semidi segment near the landward edge of the accretionary prism and the BSFZ (Fig. 1; Krabbenhoeft et al., 2021) suggests active fluid flow from areas of high pore fluid pressure to areas of lower pore fluid pressure. These fluids may then finally be drained from the system at the seafloor in the form of seafloor vents via pathways supplied by the proposed BSFZ and/or splay faults near model distance ~160 km.

Although changes in permeability between terranes in the overriding plate in the Semidi segment may influence the distribution of fluids, it is not obvious that this is a primary control on slip behavior because the abundance of fluids at depth may be limited. The crust and upper mantle of the subducting oceanic plate are not thought to be extensively hydrated based on the absence of a pronounced reduction in velocity in the subducting plate and limited outer rise seismicity and faulting (e.g., Shillington et al., 2015; Wei et al., 2021); thus the primary source of water entering the trench may be in the pores and hydrous minerals within the subducting sediment. Pore fluids would be released at much shallower depths than the 2021 Chignik earthquake (e.g., possibly along the BSFZ). The temperature structure of the Alaska megathrust is uncertain, but it is possible that metamorphic dehydration reactions (e.g., smectite to illite) in the sediments could occur at relevant depths to influence the plate boundary (Pytte & Reynolds, 1988; Abers et al, 2020).

*Possibility B:* A compilation of seismic velocities from circum-Pacific and Indian Ocean subduction zone seismic profiles suggest that landward increases in seismic velocities of the overriding plate may imply a coincident increase in the shear modulus, or rigidity, of the overriding plate material (Sallarès & Ranero, 2019). Changes in the rigidity of the overriding plate material may constitute a source of segmentation along the plate boundary such that higher rigidity material may be more capable of storing and releasing elastic strain via larger magnitudes of earthquake slip (e.g., Bassett et al., 2016).

For the Semidi segment of the Alaska subduction zone, the observed increase in seismic velocities between the Chugach and Prince William Terranes could indicate a landward increase in rigidity of the overriding plate material due to higher metamorphic grade within the Chugach Terrane. If this is the case, then it is possible that the Chugach Terrane is more capable of storing and releasing elastic strain via large earthquake rupture sourced from the deep (>25 km) plate boundary megathrust. Conversely, the less rigid material that composes the Prince William Terrane may be less capable of storing and releasing elastic strain and more likely to experience aseismic (slow) slip. This hypothesis is consistent with the occurrence of the 2021 megathrust earthquake below the Chugach Terrane and slow slip and afterslip below the Prince William Terrane (Fig. 9; Elliott et al., 2022; Liu et al., 2022; Mulia et al., 2022, He et al., 2023, Brooks et al., 2023). Similar relationships between overriding plate rigidity and slip behavior are observed from the Japan subduction zone in which interseismic locking and most co-seismic slip during the 2011 Mw9.2 Tohoku-oki earthquake appeared focused beneath a denser, more mafic, and more rigid terrane in the overriding plate (Bassett et al., 2016).

*Possibility C:* Another possibility is that megathrust behavior in the Semidi segment could be controlled by the frictional properties of the upper plate lithologies that immediately bound the megathrust. It is possible that the weakly metamorphosed sediment sequences that compose the Prince William Terrane (Horowitz et al., 1989) and overly the shallow megathrust could promote conditionally stable conditions on the shallow megathrust (<25 km). Conversely, the higher degrees of metamorphism in the Chugach Terrane (Horowitz et al., 1989) could result in unstable behavior on the deeper portions of the megathrust. This possibility is supported by the presence of more smectite clays in the Prince William terrane rocks and a greater proportion of illite in the Chugach terrane rocks where they are exposed on Kodiak (Sample & Moore, 1987). Some studies link smectite to velocity-strengthening behavior and illite to velocity weakening behavior (Oleskevich et al., 1999), although this is not consistently observed in experiments (Saffer & Marone, 2003).

Existing constraints do not allow us to definitively pinpoint the mechanism or combination of mechanisms by which the upper plate influences megathrust slip behavior. However, the spatial correspondence of overriding plate terranes and changes in slip behavior suggests that the upper plate may contribute to observed patterns of megathrust behavior.

### 6.2: Along-strike differences in upper plate structure and slip behavior

The availability of constraints on upper plate structure from wide-angle seismic data in both the strongly-coupled Semidi segment from ALEUT Line 3 presented here and farther west within the weakly-coupled Shumagin Gap along seismic profile ALEUT Line 5 (Fig. 2;

Shillington et al., 2022) provide the opportunity to compare the two. Although both the Semidi segment and the Shumagin Gap share similar large-scale thermal structure and geologic histories (Abers et al., 2020), there are a couple of important differences in overriding plate structure, implying differences in lower crustal composition and stress state (Fig. 10).

Both segments have low-velocity accretionary prisms, but this prism is much wider in the Semidi segment (~45 km) than in the Shumagin segment (~20 km). The large accretionary prism in the Semidi segment is due to a thicker sediment section on the incoming plate, including the Zodiac fan and thicker trench fill (e.g., Von Huene et al., 2012). The slip behavior of the shallow megathrust is poorly known for both segments, but the difference in outermost forearc structure shows that more competent crustal rock overlies the megathrust closer to the trench in the Shumagin Gap than in the Semidi segment, and thus the Shumagin Gap may be more prone to shallow seismic slip than the Semidi segment (Bécel et al., 2017, Li et al., 2018).

The crust in the outer forearc of both segments is interpreted to be composed of the Prince William Terrane and has similar velocities of 5-6.25 km/s, but this terrane is wider on ALEUT Line 3 (~70 km) than on ALEUT Line 5 (~50 km). Both models exhibit prominent steps in seismic velocity interpreted to separate the Prince William and Chugach terranes, but the increase in velocity is more dramatic on ALEUT Line 5. Upper crustal velocities within the interpreted Chugach terrane on both profiles are similar, ranging from 5-6.2 km/s. However, the two profiles differ markedly in lower crustal velocity. Lower crustal velocities on ALEUT Line 5 beneath both the Prince William and Chugach Terrane reach ~7.2 km/s, which have been interpreted as high-velocity, mafic intrusions into the overriding plate in this region (Shillington et al., 2022; Fig. 10). In the Chugach terrane, an abrupt increase in velocities is observed at a depth of 13 km from 5.6 to 6.4 km/s. In contrast, the Line 3 velocity model displays maximum lower crustal velocities beneath the Chugach Terrane of about 6.8 km/s and maximum velocities below the Prince William Terrane of 6 km/s (Fig. 10). Velocities increase more gradually with depth within the lower crust of the Line 3 velocity model.

Differences in lower crustal velocity and composition could have existed in terranes that form the overriding plate prior to the modern subduction and/or due to later modification of the Shumagin Gap by deformation and magmatism at the edge of the Beringian margin and westward transition to an oceanic subduction zone. Onshore geological studies suggest that the both the Chugach and Prince William terranes host Paleocene magmatic intrusions; the volume of such intrusions could be greater to the west. Alternatively or additionally, the proportion of more mafic components of the Chugach terrane could be greater in the west. The offset of high velocity material along the interpreted suture between terranes on ALEUT Line 5 (Shillington et al., 2022) suggests that at least some of the differences in lithology that lead to the differences in velocity must have developed before thrusting and accretion of the terranes.

Secondly, the overriding plate within the Shumagin Gap is located at the edge of the continental margin near the transition to an oceanic arc and is bounded to the west by NW-trending faults that parallel the ancient Beringian margin (Fig. 1; Bruns et al., 1987; Horowitz et al., 1989). A prominent, active, landward-dipping normal fault and the associated Sanak basin is imaged on ALEUT Line 5 as a part of this complex faulting in the western Alaska Peninsula; this normal fault roots into the megathrust and is interpreted to be a reactivation of the Contact Fault that separates the Prince William and Chugach terranes (Bécel et al., 2017; Shillington et al., 2022). We do not observe similar normal faulting or basins near the estimated location of the Contact Fault on ALEUT Line 3 (Kuehn, 2019) implying that the upper plate of the Semidi segment is in a compressional regime (not actively extending) and the upper plate of the

Shumagin Gap is in an extensional regime. Thus, a possible explanation for the difference in lower crustal velocities between the Semidi segment and Shumagin Gap could be more mafic intrusions into the overriding plate in the Shumagin Gap associated with observed active normal-faulting and extension of its upper plate and its proximity to complex extensional faulting to the west near the Beringian margin and transition to an oceanic subduction zone to the west.

The presence of more mafic intrusions within the Shumagin Gap could imply lower permeability, higher rigidity and/or different frictional properties along the plate boundary compared with the Semidi segment. However, both rigidity and permeability could be modulated by differences in upper plate faulting between the two segments described above. Lower permeability of the overriding plate in the Shumagin Gap compared to the Semidi segment could promote greater trapping or channelizing of fluids at depth along the plate boundary, but the observed landward-dipping normal fault at the Prince William-Chugach Terrane boundary could act as a localized pathway for fluids to travel from the plate boundary. As a result, it is unclear whether there are differences in overriding plate permeability. However, the sources and volumes of fluids being delivered to each segment differ. Much of the fluids that enter the Semidi segment are within a ~600-m-thick sediment package (Li et al., 2018), but limited bending faulting and less crustal and upper mantle hydration is inferred for the Semidi segment (Shillington et al., 2015; Wei et al., 2021). In contrast, previous studies have shown more outer-rise bending faulting and decreased crustal and mantle velocities of the incoming plate entering the Shumagin Gap, implying that the subducting plate in the Shumagin Gap is more hydrated than in the Semidi segment (Acquisto et al., 2022). The incoming plate has a thin sediment package, very little of which subducts. Thus, there could be an interplay between the source and volume fluids entering each respective subduction zone segment, heterogeneity of the megathrust due to variations in sediment input and basement roughness, and upper plate structural configurations that impact megathrust properties at depth within the seismogenic zone.

## 7. Conclusions

We used OBS data to create a P-wave velocity model of the overriding plate in the Semidi segment. Integrated with coincident multichannel seismic reflection imaging and rupture models for recent megathrust earthquakes and aseismic slip we are able to observe a spatial correspondence between overriding plate terranes and changes in megathrust slip behavior, suggesting the upper plate may contribute to observed patterns of earthquake behavior.

1. We observe large-scale P-wave velocity variations within the upper plate of the Semidi segment that could indicate major structural and lithological boundaries between upper plate domains: the modern accretionary prism (model distance 115 – 160 km), the Paleocene Prince William Terrane (model distance 160 – 220 km) and the Cretaceous Chugach Terrane (model distance 220 – 320 km).
2. Shallow slow slip (He et al., 2023) and aseismic afterslip (Brooks et al., 2023) are focused beneath the accretionary prism and the younger, lower velocity Prince William Terrane. Rupture in the 2021 earthquake (e.g., Elliot et al., 2022) is concentrated below the older, higher velocity Chugach terrane. This observed pattern could suggest upper plate influence on megathrust slip behavior due to variations in the permeability and/or rigidity of the overriding plate terranes and changes in frictional properties of overriding plate lithologies bounding the megathrust plate boundary. Existing constraints do not allow us to pinpoint one mechanism or combination of mechanisms in which the upper plate could contribute to the observed earthquake behavior.

3. Comparisons between the strongly-coupled Semidi (ALEUT Line 3 presented here) and the weakly-coupled Shumagin Gap (ALEUT Line 5; Shillington et al., 2022) display distinct differences in overriding plate structure and lower crustal velocities, implying different lower crustal compositions and stress state. Along-strike variations in upper plate structural configurations and the source and volumes of fluids entering each respective subduction zone segment could influence megathrust properties at depth.

# Figures

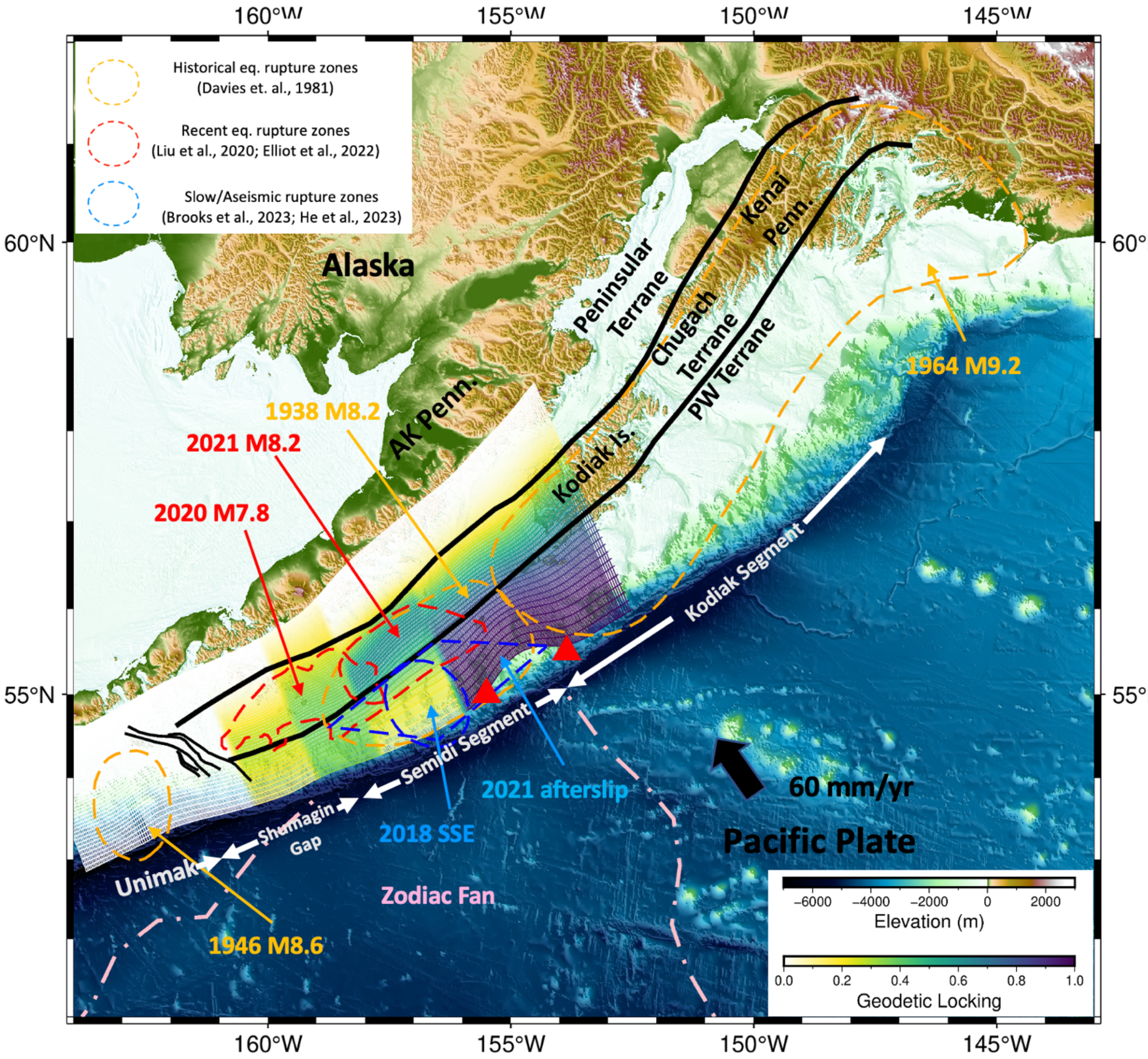

Figure 1: Map of the subduction zone offshore of the Alaska Peninsula. Shown are geodetic locking along-strike (Xiao et al., 2021), estimated rupture zones for the 2021 M8.2 Chignik earthquake (Elliot et al., 2022), 2020 M7.8 Simeonof earthquake (Liu et al., 2020), 1938 M8.2 earthquake, 1946 M8.6 earthquake, and1964 M9.2 earthquake (Davies et al., 1981), 2018 Slow Slip Event (SSE) (He et al., 2023) and aseismic afterslip (Brooks et al., 2023). Black solid lines represent NW-trending faults that bound the western Shumagin Gap (Bruns et al., 1987) and accreted overriding plate terrane domains and estimated offshore terrane boundaries (Horowitz et al., 1989) (PW Terrane = Prince William Terrane). Pink dot-dashed lines represent the Zodiac fan on the incoming Pacific Plate (Von Huene et al., 2012). Red triangles show the locations of potential seafloor vents observed in the eastern portions of the Semidi segment from acoustic backscatter images (Von Huene et al., 2021; Krabbenhoeft et al., 2021). Black arrow shows the relative motion between the subducting Pacific plate and the overriding North American plate (DeMets et al., 2010).

Table 1: List of all 21 OBS instruments deployed for ALEUT Line 3 including distance from the southernmost airgun source shot and estimated depth below sea-level from GMRT grid (Ryan et al., 2009), which includes bathymetry data from the ALEUT experiment. * Indicates OBS 314, which had timing issues and was not included in this analysis.

| OBS # | Latitude (ºN) | Longitude (ºW) | Distance along profile from southernmost shot (km) | Depth BSL (m) |
|---|---|---|---|---|
| **301** | 53.675034 | 155.50629 | 21.34 | 4502 |
| **302** | 53.800613 | 155.61761 | 37.13 | 4591 |
| **303** | 53.926205 | 155.73007 | 52.95 | 4705 |
| **304** | 54.051517 | 155.84258 | 68.73 | 4933 |
| **305** | 54.176659 | 155.95717 | 84.55 | 5169 |
| **306** | 54.275196 | 156.04573 | 96.95 | 5490 |
| **307** | 54.452320 | 156.20782 | 119.30 | 5472 |
| **308** | 54.582043 | 156.3339 | 135.89 | 4273 |
| **309** | 54.707588 | 156.44629 | 151.63 | 3039 |
| **310** | 54.831097 | 156.56203 | 167.27 | 1738 |
| **311** | 54.957924 | 156.68246 | 183.36 | 1376 |
| **312** | 55.083225 | 156.80145 | 199.25 | 474 |
| **313** | 55.207802 | 156.92204 | 215.11 | 117 |
| **314*** | 55.348305 | 156.99397 | 231.04 | 97 |
| **315** | 55.457256 | 157.16089 | 246.74 | 90 |
| **316** | 55.581020 | 157.28368 | 262.55 | 93 |
| **317** | 55.704895 | 157.40828 | 278.41 | 97 |
| **318** | 55.828449 | 157.53229 | 294.22 | 104 |

| | | | | |
|---|---|---|---|---|
| **319** | 55.952629 | 157.65569 | 310.05 | 81 |
| **320** | 56.077408 | 157.77922 | 325.93 | 166 |
| **321** | 56.200882 | 157.90663 | 341.79 | 150 |

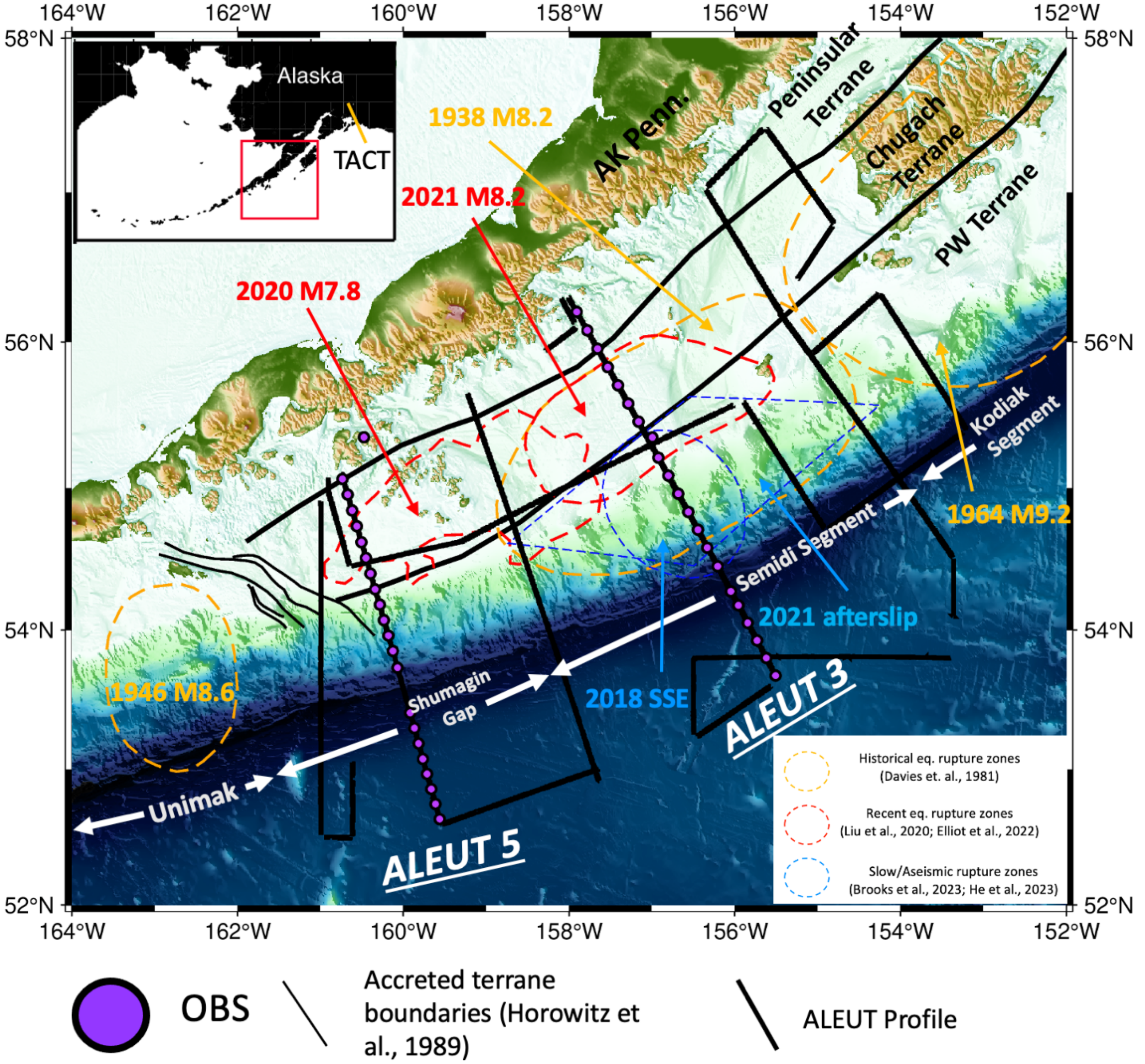

Figure 2: Map of the ALEUT experiment to image the subduction zone offshore of the Alaska Peninsula. Shown are ALEUT seismic profiles (bold black lines), Line 3 and Line 5 ocean bottom seismometer locations (purple circles). Estimated rupture zones for the 2021 M8.2 Chignik earthquake (Elliot et al., 2022), M7.8 Simeonof earthquake (Liu et al., 2020), 1938 M8.2 earthquake (Davies et al., 1981), 1964 M9.2 earthquake (Davies et al., 1981), 1946 M8.6 earthquake (Davies et al., 1981), 2018 SSE (He et al., 2023), and aseismic afterslip (Brooks et al., 2023) are shown as colored circles. Also shown are accreted terrane boundaries (solid black lines, Horowitz et al., 1989). Inset shows map location and TACT wide-angle seismic profile (orange solid line; Fuis et al., 2008) referenced in Fig. 10. AK Penn = Alaska Peninsula. PW Terrane = Prince William Terrane. SSE = Slow Slip Event.

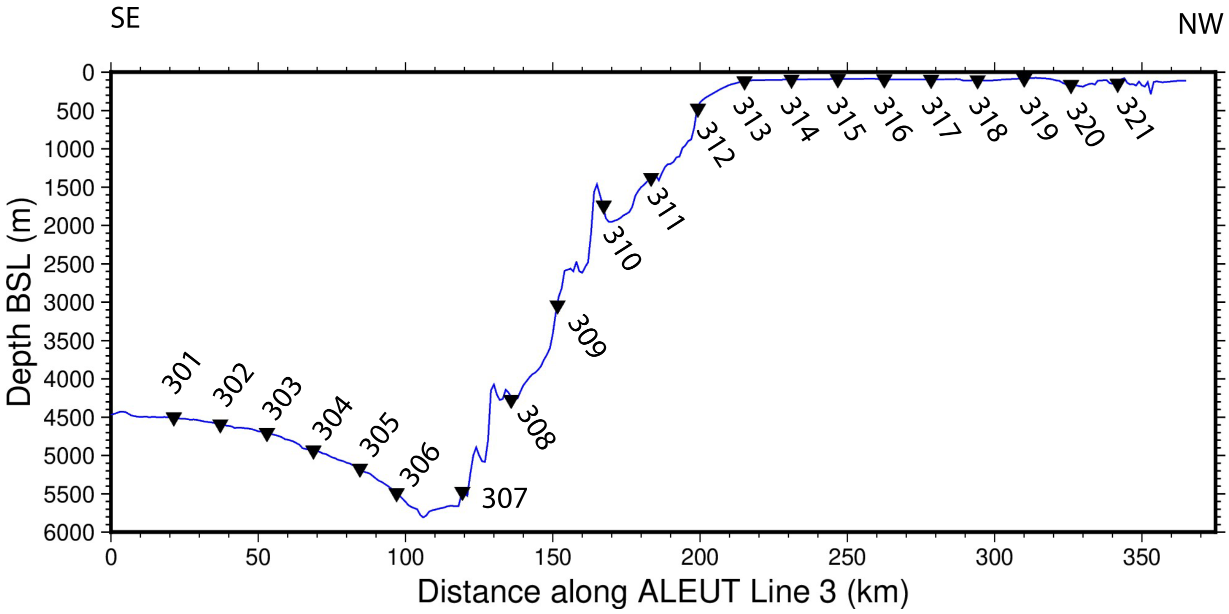

Figure 3: Plot of each OBS location along ALEUT Line 3 with respect to depth below sea level and distance along the profile. Blue line represents the seafloor and was extracted from multibeam bathymetry collected by the *R/V Langseth's* EM122 echosounder.

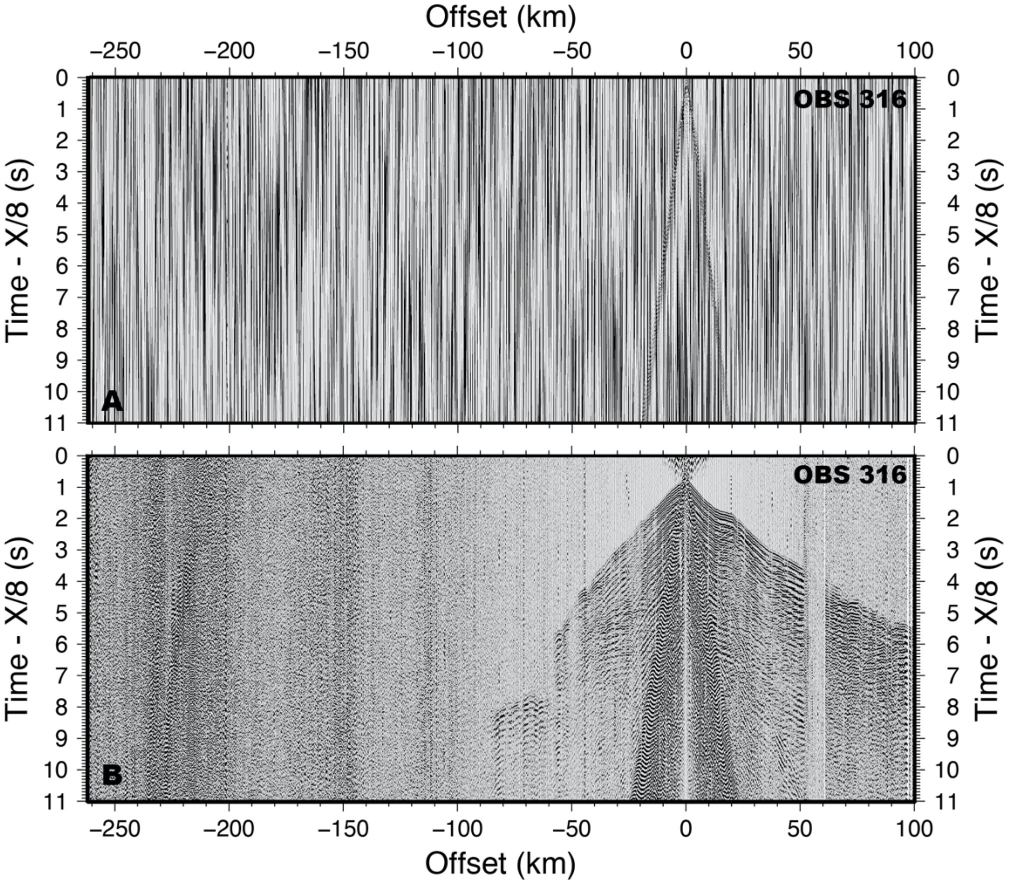

Figure 4: An example of OBS data processing on OBS 316 before (A) and after (B) application of a bandpass filter with pass corners of 3-5-15-20 Hz and an offset-dependent gain. Processed / filtered OBS data were used for arrival time picking and seismic phase identification in subsequent steps.

Table 2: Travel-time uncertainties (ms) were assigned to observed seismic phases. * indicates that both Pg_short and Pg_long are both continental crustal refractions, with differing assigned travel-time uncertainties

| Seismic Phase | Assigned Uncertainty (ms) |
|---|---|
| **Psed** | 50 |
| **Pg_short *** | 50 |
| **Pg_long *** | 75 |
| **PpbP *** | 100 |

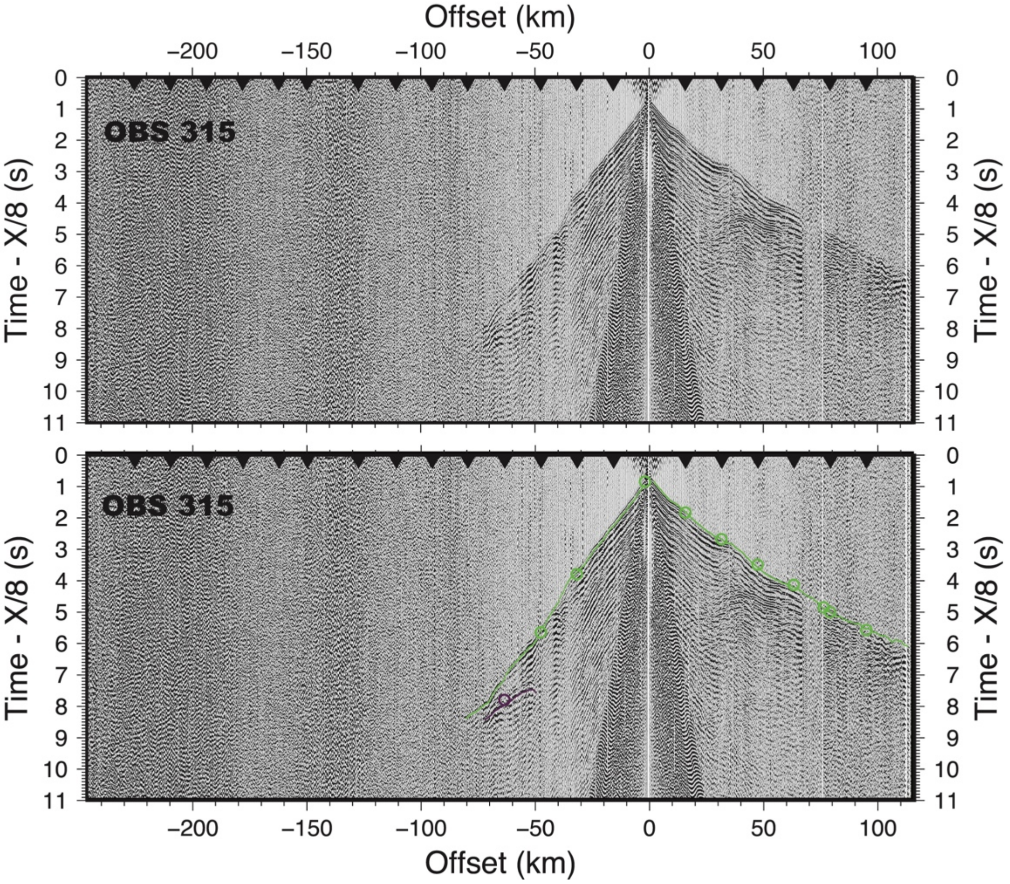

Figure 5: (Top panel) Processed seismogram for OBS 315, plotted with a reduction velocity of 8 km/s. (Bottom panel) Same seismogram with observed travel-time picks (small colored circles) and reciprocal travel-time picks from nearby OBS (large colored circles). Green colors represent continental crustal refractions (Pg_short & Pg_long), and purple colors represent plate boundary reflections (PpbP), for both observed travel-times and reciprocal travel-times. Plot demonstrates the self-consistency of seismic phase identification among different instruments. Inverted black triangles represent OBS locations along ALEUT Line 3 plotted at offsets relative to OBS 315.

Table 3: Tomographic inversion data fit statistics for the overriding plate on ALEUT Line 3. The last row reports the data fit statistics for the final average Line 3 velocity model after the Monte Carlo uncertainty analysis.

| **Seismic Phase / Final Model** | **Number of Picks** | **RMS misfit (ms)** | **Chi-squared misfit** |
|---|---|---|---|
| Psed | 131 | 59 | 2.22 |
| Pg_short & Pg_long | 4824 | 49 | 1.54 |
| PpbP | 1567 | 82 | 1.33 |
| **Final Average Model** | 6522 | 57 | 1.50 |

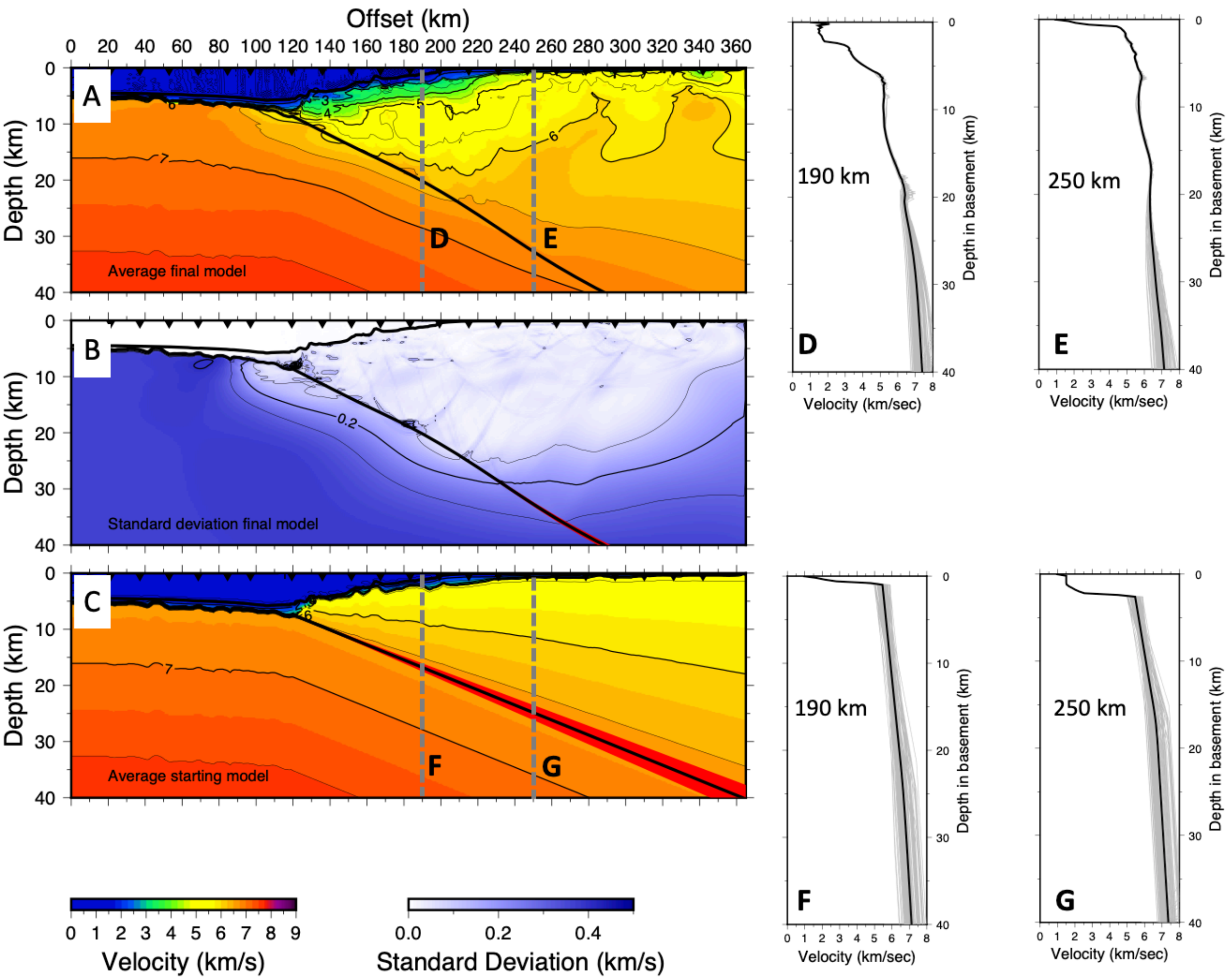

Figure 6: A.) Final average P-wave velocity model of the overriding plate along ALEUT Line 3, contoured at 0.5 km/s. B.) Standard deviation of P-wave velocities contoured at 0.1 km/s. The standard deviation of the resolved plate boundary interface depth is indicated by the thickness of the red lines. C.) Average starting model velocities contoured at 0.5 km/s, thick red line indicates the range of plate boundary geometries tested in the Monte Carlo uncertainty analysis. D-E.) 1D velocity profiles (grey lines) extracted from 100 final models used in the uncertainty analysis at model distances 190 and 250 km. Black line in both panels indicates the 1D velocity profile of the final average model at the respective model distance. F-G.) 1D velocity profiles (grey lines) extracted from 100 starting models used in the uncertainty analysis at model distances 190 and 250 km. Black line in both panels D and E indicate the 1D velocity profile of the average starting model at 190 and 250 km.

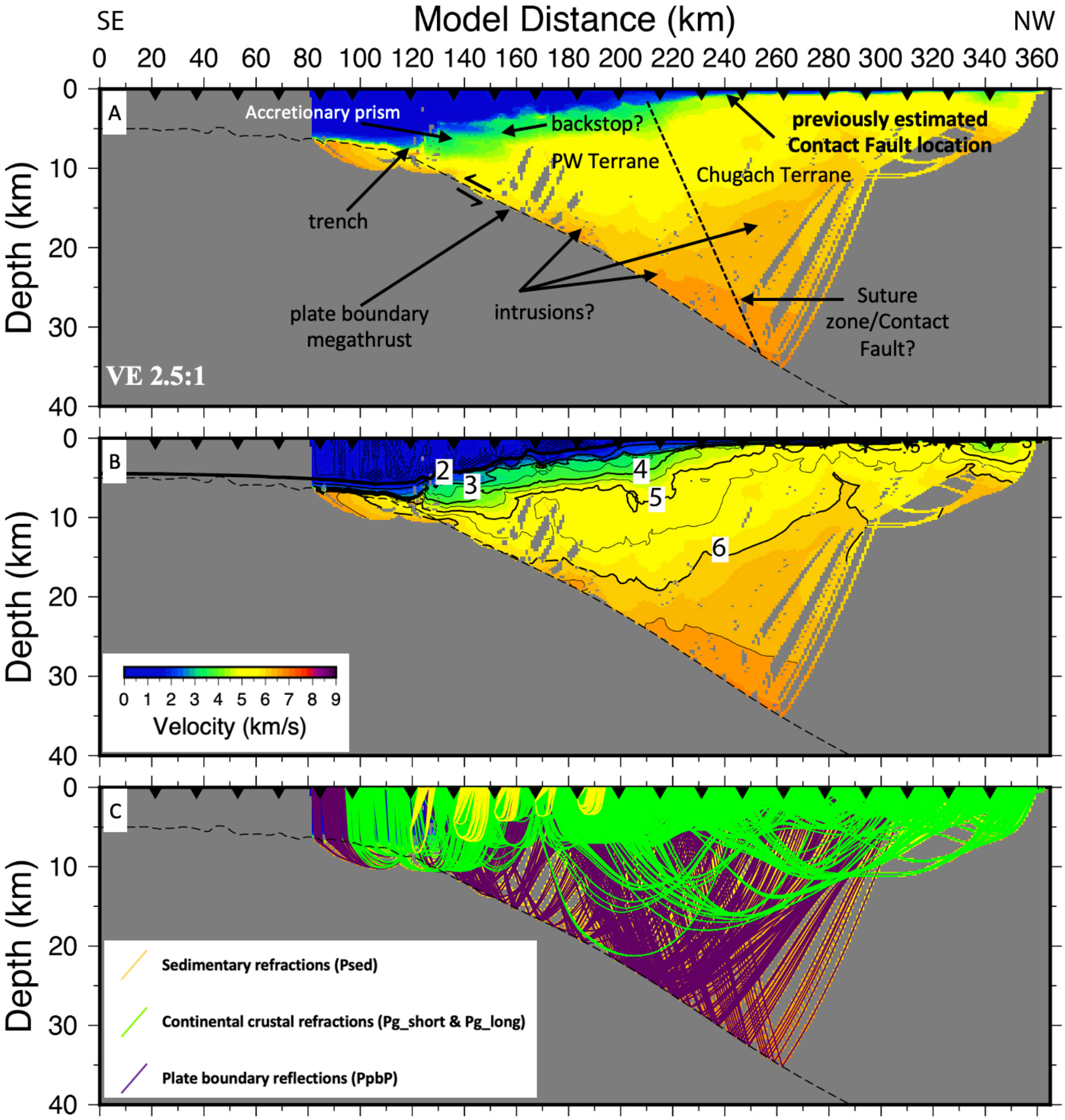

Figure 7: (A) Interpreted final average Line 3 P-wave velocity model. Gray indicates areas without ray coverage. "PW Terrane" is the Prince William Terrane. Bolded arrow indicates the approximate location of a previously estimated boundary between the Prince William and Chugach terranes (Contact Fault; Horowitz et al., 1989). (B) Final average model contoured every 0.5 km/s. (C) Ray coverage in final average model.

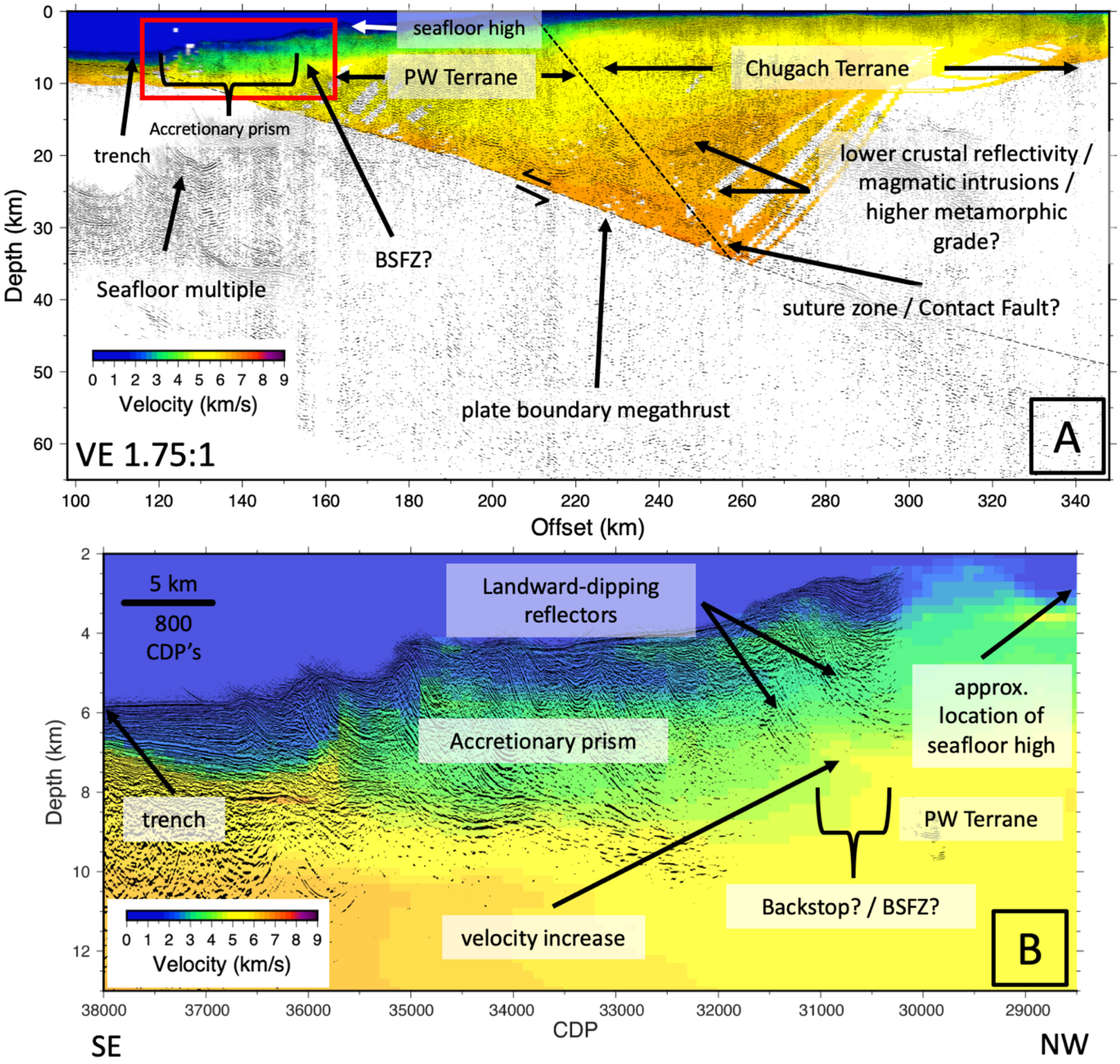

Figure 8: (A) Multichannel seismic image of ALEUT Line 3 (Kuehn, 2019) overlain on the final average Line 3 P-wave velocity model presented here and labeled with various interpretations. BSFZ = Backstop fault zone. PW Terrane = Prince William Terrane. (B) The same Line 3 velocity model overlain on a multichannel seismic image of ALEUT Line 3 (Li et al., 2018) zoomed in on the approximate Line 3 model distances of 115 km – 170 km down to 12.5 km depth outlined in the red box in panel A. The landward dipping seismic reflections shown approximately collocate with the velocity increase near the Line 3 velocity model distance 160 km and suggests the location for a BSFZ within the upper plate of the Semidi segment.

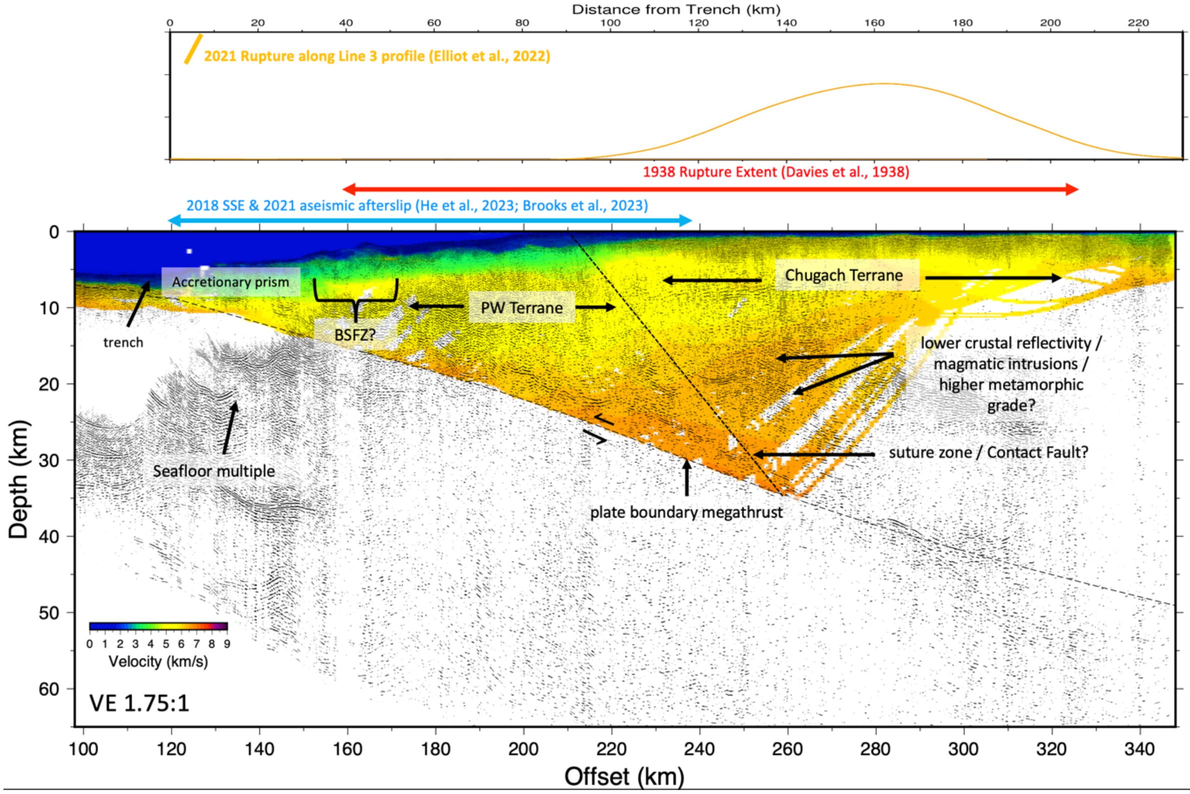

Figure 9: Multichannel seismic image of ALEUT Line 3 (Kuehn, 2019) overlain on the final average P-wave velocity model. Top panel shows the estimated rupture extents along the Line 3 profile for the 2021 earthquake (orange line; extracted from Elliot et al., 2022), the 1938 earthquake (red arrow; Davies et al., 1981), the 2018 SSE (blue arrow; He et al., 2023), and 2021 aseismic afterslip (blue arrow; Brooks et al., 2023). BSFZ = Backstop fault zone. PW Terrane = Prince William Terrane.

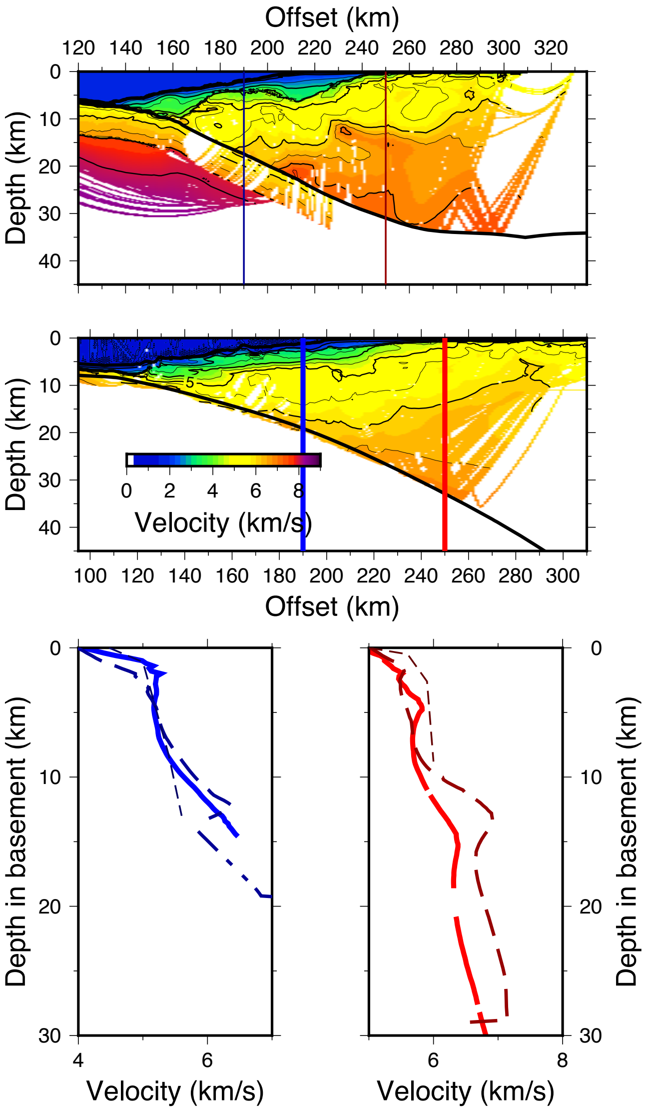

Figure 10: (Top panel) The final P-wave velocity model of the Shumagin Gap along ALEUT Line 5 (Shillington et al., 2022) contoured at 0.5 km/s. (Middle panel) The final P-wave velocity model of the central Semidi segment along ALEUT Line 3 presented here, contoured at 0.5 km/s (Left bottom panel) 1-D profiles of P-wave crustal velocities at the outer-forearc for Line 5 (thin, dashed blue line), Line 3 (thick, dashed blue line) and the TACT profile (thinnest, dashed blue line; Fuis et al., 2008) (Right bottom panel) 1-D profiles of P-wave crustal velocities at a location more landwards within the overriding plate Line 5 (thin, dashed red line), Line 3 (thick, dashed red line) and the TACT profile (thinnest, dashed red line; Fuis et al., 2008). Location of TACT profile shown in inset of Fig. 2).

# References

Abers, G. A., van Keken, P. E., & Wilson, C. R. (2020). Deep decoupling in subduction zones: Observations and temperature limits. *Geosphere*, *16*(6), 1408–1424. https://doi.org/10.1130/GES02278.1

Acquisto, T., Bécel, A., Singh, S. C., & Carton, H. (2022). Evidence of Strong Upper Oceanic Crustal Hydration Outboard the Alaskan and Sumatran Subduction Zones. *Journal of Geophysical Research: Solid Earth*, *127*(10), e2022JB024751. https://doi.org/10.1029/2022JB024751

Araki, E., Saffer, D. M., Kopf, A. J., Wallace, L. M., Kimura, T., Machida, Y., et al. (2017). Recurring and triggered slow-slip events near the trench at the Nankai Trough subduction megathrust. *Science*, *356*(6343), 1157–1160. https://doi.org/10.1126/science.aan3120

Audet, P., Bostock, M. G., Christensen, N. I., & Peacock, S. M. (2009). Seismic evidence for overpressured subducted oceanic crust and megathrust fault sealing. *Nature*, *457*(7225), 76–78. https://doi.org/10.1038/nature07650

Bassett, D., Sandwell, D. T., Fialko, Y., & Watts, A. B. (2016). Upper-plate controls on co-seismic slip in the 2011 magnitude 9.0 Tohoku-oki earthquake. *Nature*, *531*(7592), 92–96. https://doi.org/10.1038/nature16945

Bécel, A., Shillington, D. J., Delescluse, M., Nedimović, M. R., Abers, G. A., Saffer, D. M., et al. (2017). Tsunamigenic structures in a creeping section of the Alaska subduction zone. *Nature Geoscience*, *10*(8), 609–613. https://doi.org/10.1038/ngeo2990

Bekins, B., McCaffrey, A. M., & Dreiss, S. J. (1994). Influence of kinetics on the smectite to illite transition in the Barbados accretionary prism. *Journal of Geophysical Research: Solid Earth*, *99*(B9), 18147–18158. https://doi.org/10.1029/94JB01187

Braden, Z., & Behr, W. M. (2021). Weakening Mechanisms in a Basalt-Hosted Subduction Megathrust Fault Segment, Southern Alaska. *Journal of Geophysical Research: Solid Earth*, *126*(9). https://doi.org/10.1029/2021JB022039

Brooks, B. A., Goldberg, D., DeSanto, J., Ericksen, T. L., Webb, S. C., Nooner, S. L., et al. (2023). Rapid shallow megathrust afterslip from the 2021 M8.2 Chignik, Alaska earthquake revealed by seafloor geodesy. *Science Advances*, *9*(17), eadf9299. https://doi.org/10.1126/sciadv.adf9299

Bruns, T. R., Von Huene, R., Culotta, R. C., Lewis, S. D., & Ladd, J. W. (1987). Geology and Petroleum potential of the Shumagin margin, Alaska. In Geology and resource potential of the Western North America and adjacent ocean basins-Beaufort Sea to Baja California (Vol. 6, pp. 157–189).

Calvert, A. J., & McGeary, S. E. (2013). Seismic reflection imaging of ultradeep roots beneath the eastern Aleutian island arc. *Geology*, *41*(2), 203–206. https://doi.org/10.1130/G33683.1

Christensen, N. I., & Mooney, W. D. (1995). Seismic velocity structure and composition of the continental crust: A global view. *Journal of Geophysical Research: Solid Earth*, *100*(B6), 9761–9788. https://doi.org/10.1029/95JB00259

Cohen, J.K., Stockwell, J.S.W., 2004. CWP/SU: Seismic Un*x Release No. 38: an open source software package for seismic research and processing. Center for Wave Phenomena, Colorado School of Mines.

Davies, J., Sykes, L., House, L., & Jacob, K. (1981). Shumagin Seismic Gap, Alaska Peninsula: History of great earthquakes, tectonic setting, and evidence for high seismic potential.

*Journal of Geophysical Research*, *86*(B5), 3821. https://doi.org/10.1029/JB086iB05p03821

DeMets, C., Gordon, R. G., & Argus, D. F. (2010). Geologically current plate motions. *Geophysical Journal International*, *181*(1), 1–80. https://doi.org/10.1111/j.1365-246X.2009.04491.x

Drooff, C., & Freymueller, J. T. (2021). New Constraints on Slip Deficit on the Aleutian Megathrust and Inflation at Mt. Veniaminof, Alaska From Repeat GPS Measurements. *Geophysical Research Letters*, *48*(4). https://doi.org/10.1029/2020GL091787

Elliott, J. L., Grapenthin, R., Parameswaran, R. M., Xiao, Z., Freymueller, J. T., & Fusso, L. (2022). Cascading rupture of a megathrust. *Science Advances*, *8*(18), eabm4131. https://doi.org/10.1126/sciadv.abm4131

Estabrook, C. H., Jacob, K. H., & Sykes, L. R. (1994). Body wave and surface wave analysis of large and great earthquakes along the Eastern Aleutian Arc, 1923-1993: Implications for future events. *Journal of Geophysical Research: Solid Earth*, *99*(B6), 11643–11662. https://doi.org/10.1029/93JB03124

Freymueller, J. T., Suleimani, E. N., & Nicolsky, D. J. (2021). Constraints on the Slip Distribution of the 1938 M $_W$ 8.3 Alaska Peninsula Earthquake From Tsunami Modeling. *Geophysical Research Letters*, *48*(9). https://doi.org/10.1029/2021GL092812

Fuis, G. S., Moore, T. E., Plafker, G., Brocher, T. M., Fisher, M. A., Mooney, W. D., et al. (2008). Trans-Alaska Crustal Transect and continental evolution involving subduction underplating and synchronous foreland thrusting. *Geology*, *36*(3), 267. https://doi.org/10.1130/G24257A.1

Fulton, P. M., & Harris, R. N. (2012). Thermal considerations in inferring frictional heating from vitrinite reflectance and implications for shallow coseismic slip within the Nankai Subduction Zone. *Earth and Planetary Science Letters*, *335–336*, 206–215. https://doi.org/10.1016/j.epsl.2012.04.012

Hayes, G. P., Moore, G. L., Portner, D. E., Hearne, M., Flamme, H., Furtney, M., & Smoczyk, G. M. (2018). Slab2, a comprehensive subduction zone geometry model. *Science*, *362*(6410), 58–61. https://doi.org/10.1126/science.aat4723

He, B., Wei, X., Wei, M., Shen, Y., Alvarez, M., & Schwartz, S. Y. (2023). A shallow slow slip event in 2018 in the Semidi segment of the Alaska subduction zone detected by machine learning. *Earth and Planetary Science Letters*, *612*, 118154. https://doi.org/10.1016/j.epsl.2023.118154

Hilley, G. E. (ed.), Brodsky, E. E., Roman, D., Shillington, D. J., Brudzinski, M., Behn, M. Tobin, H. and the SZ4D RCN (2022). SZ4D Implementation Plan. Stanford Digital Repository. Available at https://purl.stanford.edu/hy589fc7561. https://doi.org/10.25740/hy589fc7561

Horning, G., Canales, J. P., Carbotte, S. M., Han, S., Carton, H., Nedimović, M. R., & Keken, P. E. (2016). A 2-D tomographic model of the Juan de Fuca plate from accretion at axial seamount to subduction at the Cascadia margin from an active source ocean bottom seismometer survey. *Journal of Geophysical Research: Solid Earth*, *121*(8), 5859–5879. https://doi.org/10.1002/2016JB013228

Horowitz, W. L., Steffy, D. A., & Hoose, P. J. (1989). Geologic report for the Shumagin Planning Area, Western Gulf of Alaska, OCS Report, MMS 89-0097. U.S. Department of the Interior, Minerals Management Service, Alaska OCS Region.

Johnson, J. M., & Satake, K. (1994). Rupture extent of the 1938 Alaskan earthquake as inferred from tsunami waveforms. *Geophysical Research Letters*, *21*(8), 733–736. https://doi.org/10.1029/94GL00333

Kimura, G., Nakamura, Y., Shiraishi, K., Fujie, G., Kodaira, S., Tsuji, T., et al. (2022). Nankai Forearc Structural and Seismogenic Segmentation Caused by a Magmatic Intrusion off the Kii Peninsula. *Geochemistry, Geophysics, Geosystems*, *23*(8). https://doi.org/10.1029/2022GC010331

Knapp, J. H., Diaconescu, C. C., Bader, M. A., Sokolov, V. B., Kashubin, S. N., & Rybalka, A. V. (1998). Seismic reflection fabrics of continental collision and post-orogenic extension in the Middle Urals, central Russia. *Tectonophysics*, *288*(1–4), 115–126. https://doi.org/10.1016/S0040-1951(97)00288-6

Korenaga, J., Holbrook, W. S., Kent, G. M., Kelemen, P. B., Detrick, R. S., Larsen, H.-C., et al. (2000). Crustal structure of the southeast Greenland margin from joint refraction and reflection seismic tomography. *Journal of Geophysical Research: Solid Earth*, *105*(B9), 21591–21614. https://doi.org/10.1029/2000JB900188

Krabbenhoeft, A., von Huene, R., Miller, J. J., & Klaeschen, D. (2021). Subducting oceanic basement roughness impacts on upper-plate tectonic structure and a backstop splay fault zone activated in the southern Kodiak aftershock region of the Mw 9.2, 1964 megathrust rupture, Alaska. *Geosphere*, *17*(2), 409–437. https://doi.org/10.1130/GES02275.1

Kuehn, H. (2019). Along-trench segmentation and down-dip limit of the seismogenic zone at the eastern Alaska-Aleutian subduction zone (Ph.D. thesis) (p. 334). Dalhousie University.

Lay, T., Kanamori, H., Ammon, C. J., Koper, K. D., Hutko, A. R., Ye, L., et al. (2012). Depth-varying rupture properties of subduction zone megathrust faults: MEGATHRUST

RUPTURE DOMAINS. *Journal of Geophysical Research: Solid Earth*, *117*(B4), n/a-n/a. https://doi.org/10.1029/2011JB009133

Li, J., Shillington, D. J., Saffer, D. M., Bécel, A., Nedimović, M. R., Kuehn, H., et al. (2018). Connections between subducted sediment, pore-fluid pressure, and earthquake behavior along the Alaska megathrust. *Geology*, *46*(4), 299–302. https://doi.org/10.1130/G39557.1

Li, S., & Freymueller, J. T. (2018). Spatial Variation of Slip Behavior Beneath the Alaska Peninsula Along Alaska-Aleutian Subduction Zone. *Geophysical Research Letters*, *45*(8), 3453–3460. https://doi.org/10.1002/2017GL076761

Liu, C., Lay, T., & Xiong, X. (2022). The 29 July 2021 $M_W$ 8.2 Chignik, Alaska Peninsula Earthquake Rupture Inferred From Seismic and Geodetic Observations: Re-Rupture of the Western 2/3 of the 1938 Rupture Zone. *Geophysical Research Letters*, *49*(4). https://doi.org/10.1029/2021GL096004

Miller, P. K., Saffer, D. M., Abers, G. A., Shillington, D. J., Bécel, A., Li, J., & Bate, C. (2021). P- and S-Wave Velocities of Exhumed Metasediments From the Alaskan Subduction Zone: Implications for the In Situ Conditions Along the Megathrust. *Geophysical Research Letters*, *48*(20). https://doi.org/10.1029/2021GL094511

Mulia, I. E., Gusman, A. R., Heidarzadeh, M., & Satake, K. (2022). Sensitivity of Tsunami Data to the Up-Dip Extent of the July 2021 Mw 8.2 Alaska Earthquake. *Seismological Research Letters*, *93*(4), 1992–2003. https://doi.org/10.1785/0220210359

Oleskevich, D. A., Hyndman, R. D., & Wang, K. (1999). The updip and downdip limits to great subduction earthquakes: Thermal and structural models of Cascadia, south Alaska, SW Japan, and Chile. *Journal of Geophysical Research: Solid Earth*, *104*(B7), 14965–14991. https://doi.org/10.1029/1999JB900060

Plafker, George, and Berg, H.C., eds., 1994, The Geology of Alaska: Geological Society of America, 1068 p.

Pytte, A.M.; Reynolds, R.C., 1988. The thermal transformation of smectite to illite, in: T.H. McCulloh, N.D. Naeser (Eds.) Thermal Histories of Sedimentary Basins, Springer, New York, pp 133-140.

Ranero, C. R., Grevemeyer, I., Sahling, H., Barckhausen, U., Hensen, C., Wallmann, K., et al. (2008). Hydrogeological system of erosional convergent margins and its influence on tectonics and interplate seismogenesis: CONVERGENT MARGINS AND TECTONICS. *Geochemistry, Geophysics, Geosystems*, *9*(3), n/a-n/a. https://doi.org/10.1029/2007GC001679

Ryan, W. B. F., Carbotte, S. M., Coplan, J. O., O'Hara, S., Melkonian, A., Arko, R., et al. (2009). Global Multi-Resolution Topography synthesis: GLOBAL MULTI-RESOLUTION TOPOGRAPHY SYNTHESIS. *Geochemistry, Geophysics, Geosystems*, *10*(3), n/a-n/a. https://doi.org/10.1029/2008GC002332

Saffer, D. M., & Marone, C. (2003). Comparison of smectite- and illite-rich gouge frictional properties: application to the updip limit of the seismogenic zone along subduction megathrusts. *Earth and Planetary Science Letters*, *215*(1–2), 219–235. https://doi.org/10.1016/S0012-821X(03)00424-2

Saffer, D. M., & Tobin, H. J. (2011). Hydrogeology and Mechanics of Subduction Zone Forearcs: Fluid Flow and Pore Pressure. *Annual Review of Earth and Planetary Sciences*, *39*(1), 157–186. https://doi.org/10.1146/annurev-earth-040610-133408

Saffer, D. M., & Wallace, L. M. (2015). The frictional, hydrologic, metamorphic and thermal habitat of shallow slow earthquakes. *Nature Geoscience*, *8*(8), 594–600. https://doi.org/10.1038/ngeo2490

Sahling, H., Masson, D. G., Ranero, C. R., Hühnerbach, V., Weinrebe, W., Klaucke, I., et al. (2008). Fluid seepage at the continental margin offshore Costa Rica and southern Nicaragua: CONTINENTAL MARGIN FLUID SEEPAGE. *Geochemistry, Geophysics, Geosystems*, *9*(5), n/a-n/a. https://doi.org/10.1029/2008GC001978

Sallarès, V., & Ranero, C. R. (2019). Upper-plate rigidity determines depth-varying rupture behaviour of megathrust earthquakes. *Nature*, *576*(7785), 96–101. https://doi.org/10.1038/s41586-019-1784-0

Sample, J. C., & Moore, J. C. (1987). Structural style and kinematics of an underplated slate belt, Kodiak and adjacent islands, Alaska. *Geological Society of America Bulletin*, *99*(1), 7. https://doi.org/10.1130/0016-7606(1987)99<7:SSAKOA>2.0.CO;2

Scholz, C. H. (1998). Earthquakes and friction laws. *Nature*, *391*(6662), 37–42. https://doi.org/10.1038/34097

Shillington, D. J., Bécel, A., Nedimović, M. R., Kuehn, H., Webb, S. C., Abers, G. A., et al. (2015). Link between plate fabric, hydration and subduction zone seismicity in Alaska. *Nature Geoscience*, *8*(12), 961–964. https://doi.org/10.1038/ngeo2586

Shillington, D. J., Bécel, A., & Nedimović, M. R. (2022). Upper Plate Structure and Megathrust Properties in the Shumagin Gap Near the July 2020 M7.8 Simeonof Event. *Geophysical Research Letters*, *49*(2). https://doi.org/10.1029/2021GL096974

Stevenson, A. J., Scholl, D. W., & Vallier, T. L. (1983). Tectonic and geologic implications of the Zodiac fan, Aleutian Abyssal Plain, northeast Pacific. *Geological Society of America*

*Bulletin*, *94*(2), 259. https://doi.org/10.1130/0016-7606(1983)94<259:TAGIOT>2.0.CO;2

Sykes, L. R. (1971). Aftershock zones of great earthquakes, seismicity gaps, and earthquake prediction for Alaska and the Aleutians. *Journal of Geophysical Research*, *76*(32), 8021–8041. https://doi.org/10.1029/JB076i032p08021

Tape, C., & Lomax, A. (2022). Aftershock Regions of Aleutian-Alaska Megathrust Earthquakes, 1938–2021. *Journal of Geophysical Research: Solid Earth*, *127*(7). https://doi.org/10.1029/2022JB024336

Von Huene, R., Miller, J. J., & Weinrebe, W. (2012). Subducting plate geology in three great earthquake ruptures of the western Alaska margin, Kodiak to Unimak. *Geosphere*, *8*(3), 628–644. https://doi.org/10.1130/GES00715.1

Von Huene, Ronald, Miller, J. J., & Dartnell, P. (2016). A possible transoceanic tsunami directed toward the U.S. west coast from the Semidi segment, Alaska convergent margin. *Geochemistry, Geophysics, Geosystems*, 15. https://doi.org/10.1002/2015GC006147

Von Huene, R., Miller, J. J., & Krabbenhoeft, A. (2019). The Shumagin seismic gap structure and associated tsunami hazards, Alaska convergent margin. *Geosphere*, *15*(2), 324–341. https://doi.org/10.1130/GES01657.1

Von Huene, Ronald, Miller, J. J., & Krabbenhoeft, A. (2021). The Alaska Convergent Margin Backstop Splay Fault Zone, a Potential Large Tsunami Generator Between the Frontal Prism and Continental Framework. *Geochemistry, Geophysics, Geosystems*, 24. https://doi. org/10.1029/2019GC008901

Wallace, L. M., Fagereng, A., & Ellis, S. (2012). Upper plate tectonic stress state may influence interseismic coupling on subduction megathrusts. *Geology*, *40*(10), 895–898. https://doi.org/10.1130/G33373.1

Wallace, W. K., & Engebretson, D. C. (1984). Relationships between plate motions and Late Cretaceous to Paleogene magmatism in southwestern Alaska. *Tectonics*, *3*(2), 295–315. https://doi.org/10.1029/TC003i002p00295

Wang, K., & Bilek, S. L. (2014). Invited review paper: Fault creep caused by subduction of rough seafloor relief. *Tectonophysics*, *610*, 1–24. https://doi.org/10.1016/j.tecto.2013.11.024

Wei, S. S., Ruprecht, P., Gable, S. L., Huggins, E. G., Ruppert, N., Gao, L., & Zhang, H. (2021). Along-strike variations in intermediate-depth seismicity and arc magmatism along the Alaska Peninsula. *Earth and Planetary Science Letters*, *563*, 116878. https://doi.org/10.1016/j.epsl.2021.116878

Xiao, Z., Freymueller, J. T., Grapenthin, R., Elliott, J. L., Drooff, C., & Fusso, L. (2021). The deep Shumagin gap filled: Kinematic rupture model and slip budget analysis of the 2020 Mw 7.8 Simeonof earthquake constrained by GNSS, global seismic waveforms, and floating InSAR. *Earth and Planetary Science Letters*, *576*, 117241. https://doi.org/10.1016/j.epsl.2021.117241

Ye, L., Bai, Y., Si, D., Lay, T., Cheung, K. F., & Kanamori, H. (2022). Rupture Model for the 29 July 2021 $M_W$ 8.2 Chignik, Alaska Earthquake Constrained by Seismic, Geodetic, and Tsunami Observations. *Journal of Geophysical Research: Solid Earth*, *127*(7). https://doi.org/10.1029/2021JB023676

Zelt, C. A. (1999). Modelling strategies and model assessment for wide-angle seismic traveltime data. *Geophysical Journal International*, *139*(1), 183–204. https://doi.org/10.1046/j.1365-246X.1999.00934.x

# 9. Appendix

Here we show additional plots of processed seismograms for OBS 307 – 321. For figures A1 – A14 we display processed seismograms plotted with a reduction velocity of 8 km/s in the top panel. In the bottom panel of each plot we show the same seismogram plotted with observed travel-time picks (small colored circles) and reciprocal travel-time picks from nearby OBS (large colored circles). For each plot the yellow colors represent sedimentary refractions (Psed; only observed on OBS 307-311), green colors represent continental crustal refractions (Pg_short & Pg_long; Pg_long only observed on the most landward OBS), and purple colors represent plate boundary reflections (PpbP) for both observed travel-times and reciprocal travel-times. The inverted black triangles shown in both panels represent OBS locations along ALEUT Line 3 plotted at offsets relative to the OBS shown in the figure.

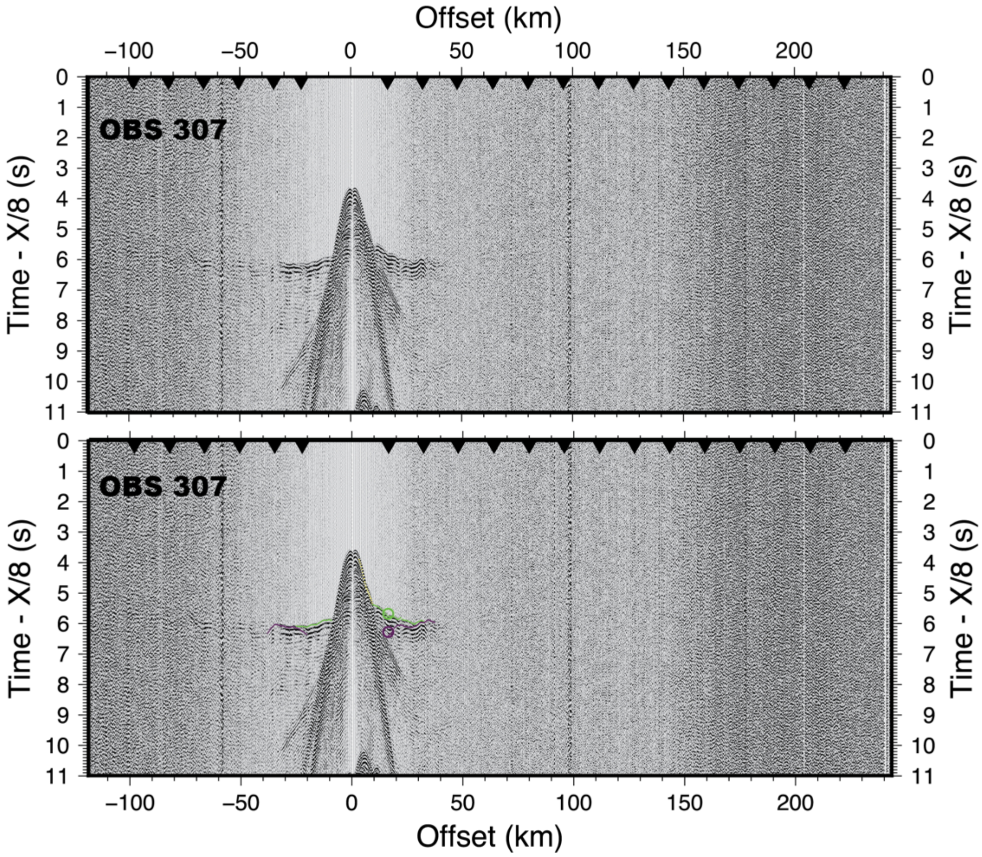

Figure A1: (Top panel) Processed seismogram for OBS 307, plotted with a reduction velocity of 8 km/s. (Bottom panel) Same seismogram with observed travel-time picks (small colored circles) and reciprocal travel-time picks from nearby OBS (large colored circles). See appendix text for color/seismic phase descriptions.

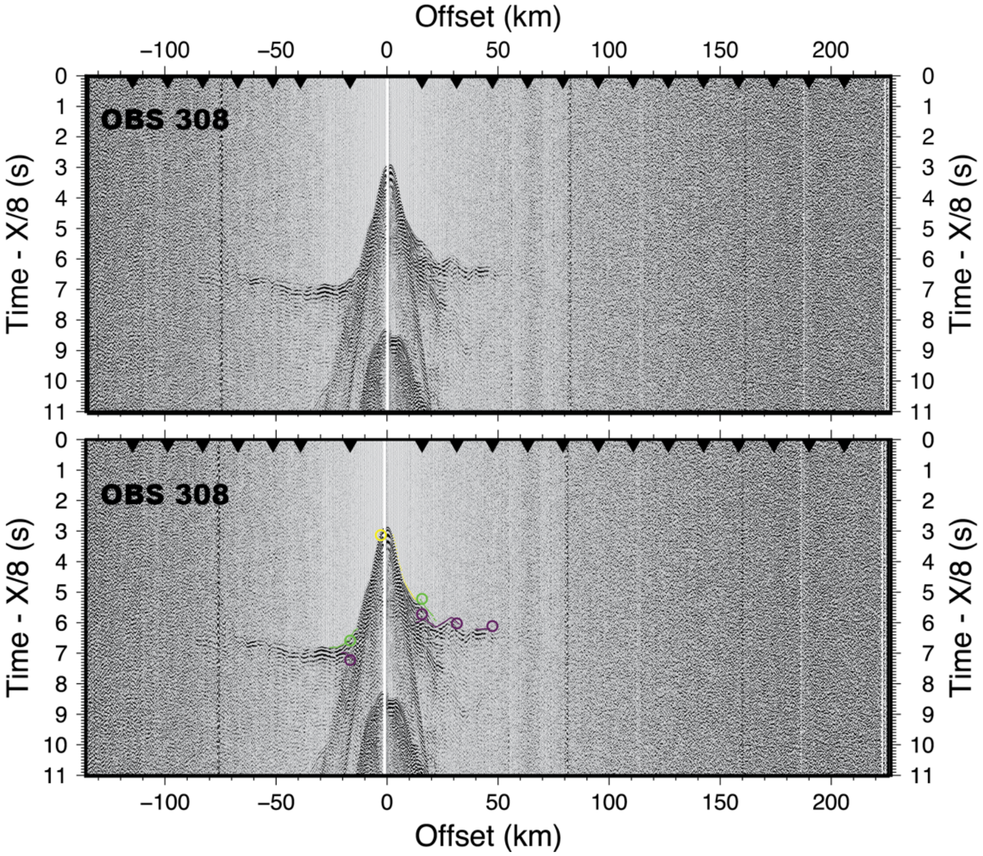

Figure A2: (Top panel) Processed seismogram for OBS 308, plotted with a reduction velocity of 8 km/s. (Bottom panel) Same seismogram with observed travel-time picks (small colored circles) and reciprocal travel-time picks from nearby OBS (large colored circles). See appendix text for color/seismic phase descriptions.

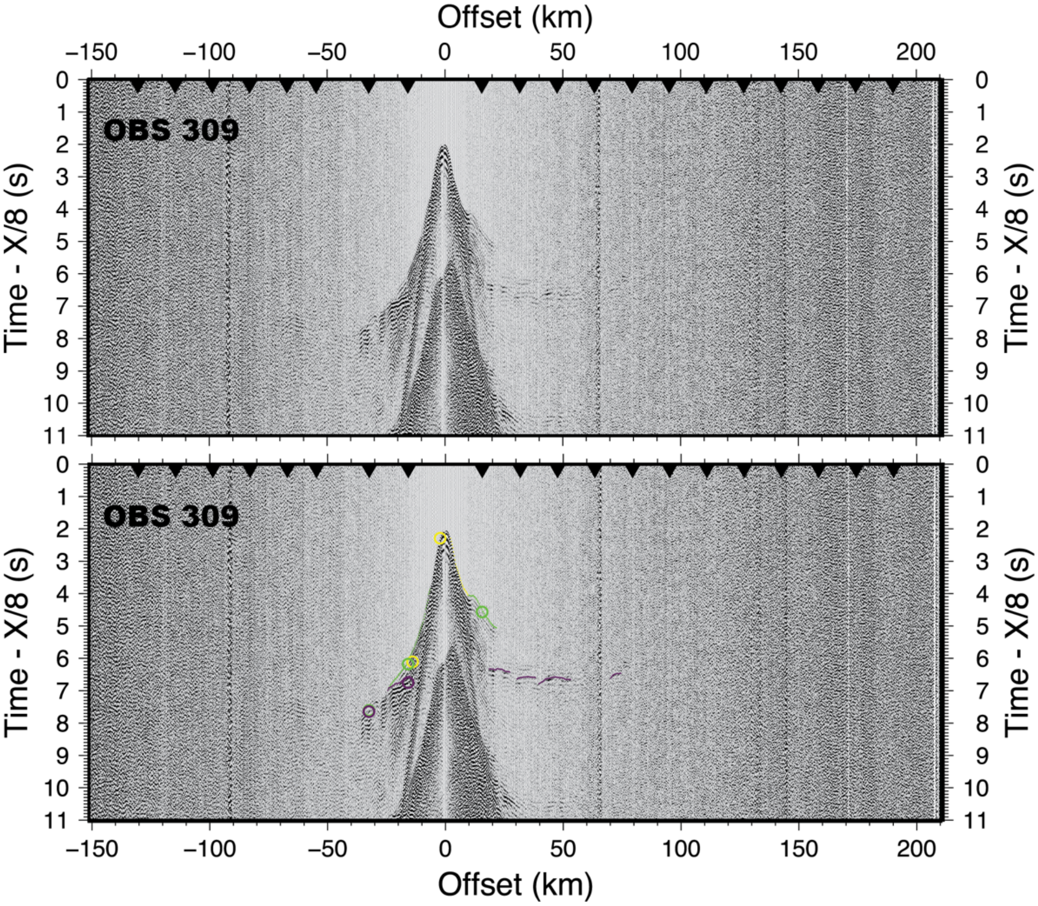

Figure A3: (Top panel) Processed seismogram for OBS 309, plotted with a reduction velocity of 8 km/s. (Bottom panel) Same seismogram with observed travel-time picks (small colored circles) and reciprocal travel-time picks from nearby OBS (large colored circles). See appendix text for color/seismic phase descriptions.

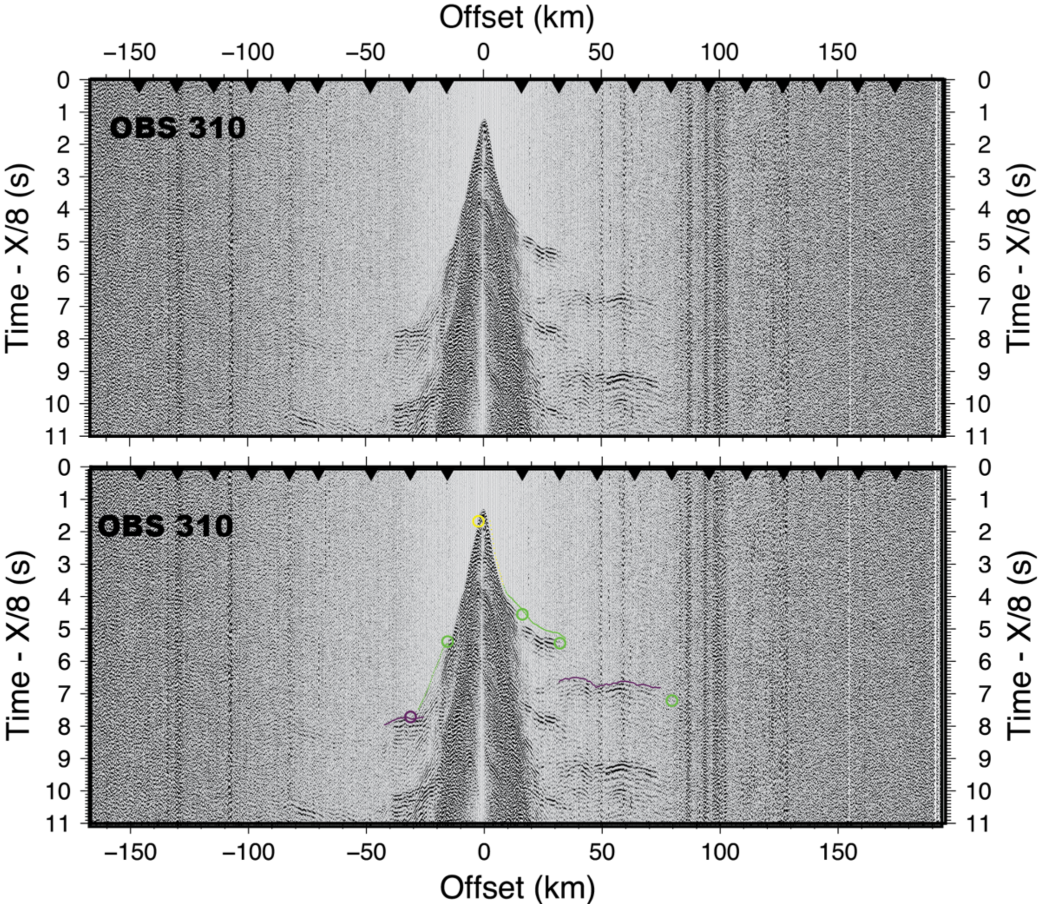

Figure A4: (Top panel) Processed seismogram for OBS 310, plotted with a reduction velocity of 8 km/s. (Bottom panel) Same seismogram with observed travel-time picks (small colored circles) and reciprocal travel-time picks from nearby OBS (large colored circles). See appendix text for color/seismic phase descriptions.

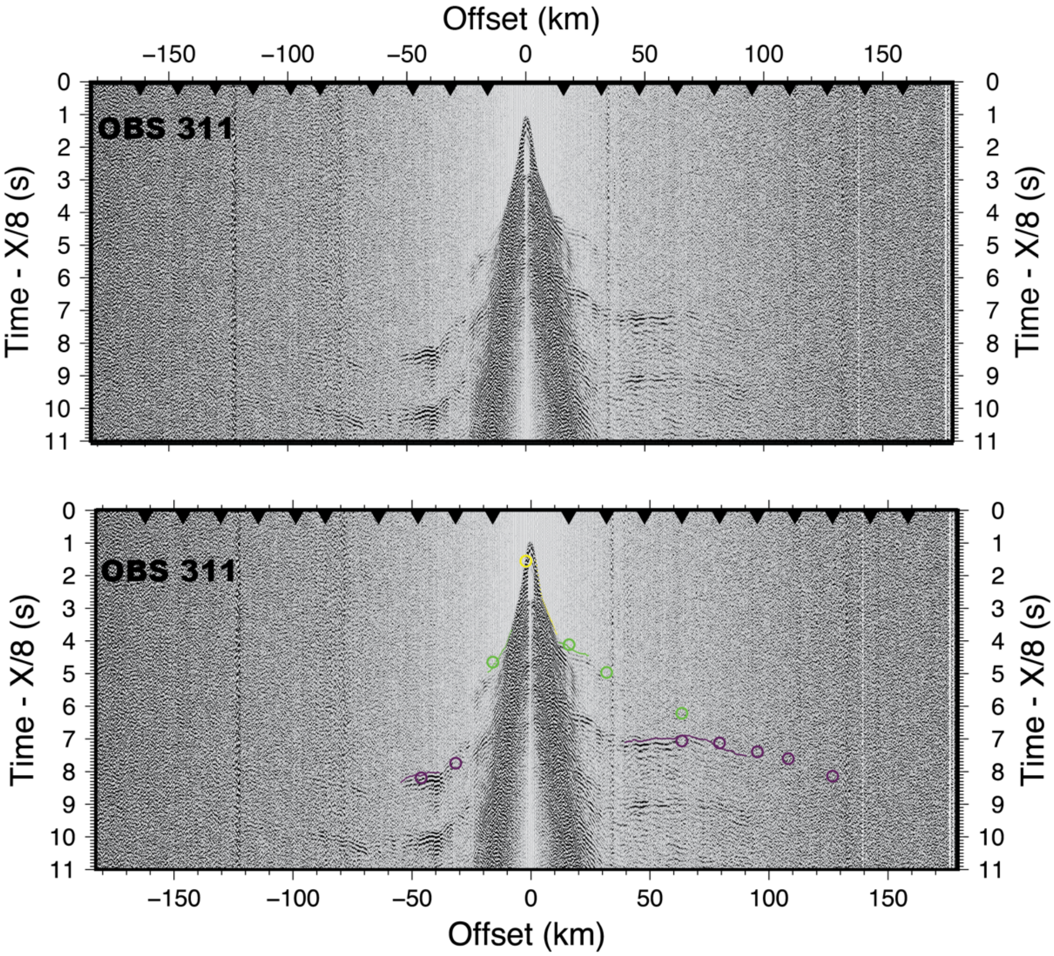

Figure A5: (Top panel) Processed seismogram for OBS 311, plotted with a reduction velocity of 8 km/s. (Bottom panel) Same seismogram with observed travel-time picks (small colored circles) and reciprocal travel-time picks from nearby OBS (large colored circles). See appendix text for color/seismic phase descriptions.

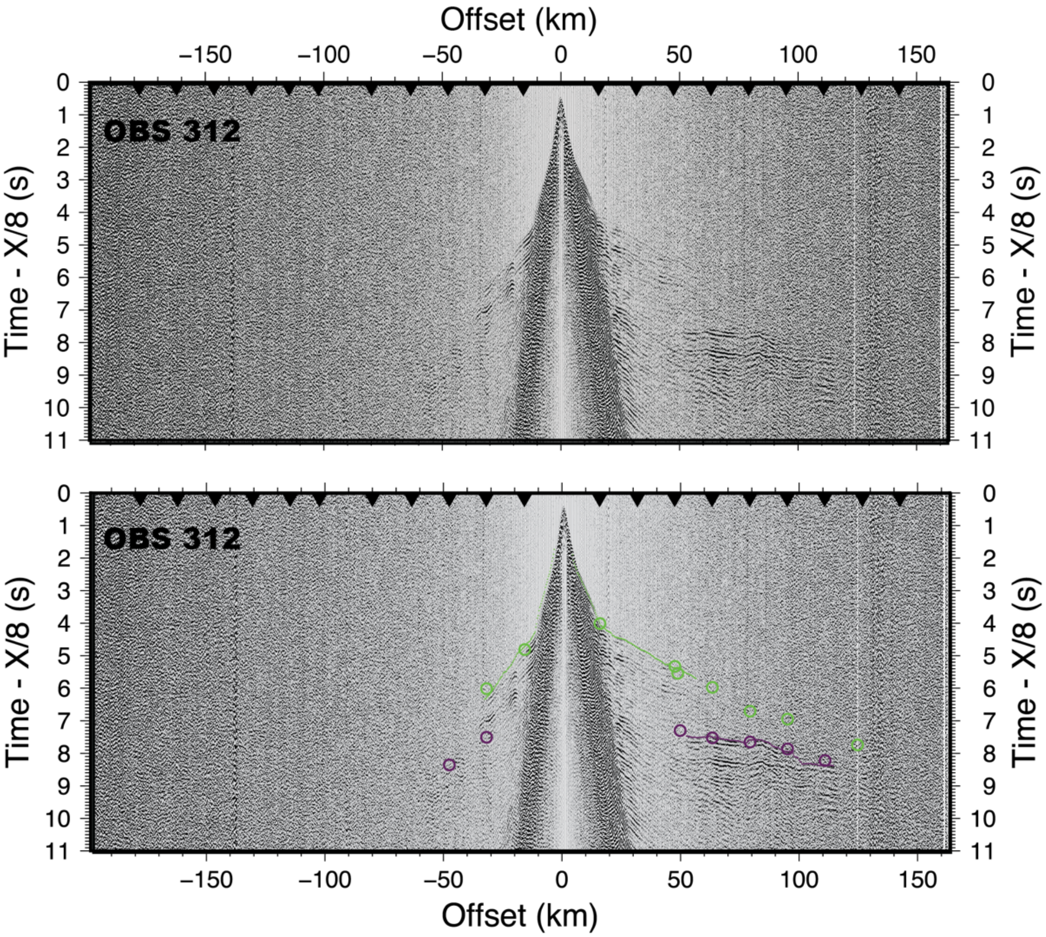

<u>Figure A6</u>: (Top panel) Processed seismogram for OBS 312, plotted with a reduction velocity of 8 km/s. (Bottom panel) Same seismogram with observed travel-time picks (small colored circles) and reciprocal travel-time picks from nearby OBS (large colored circles). See appendix text for color/seismic phase descriptions.

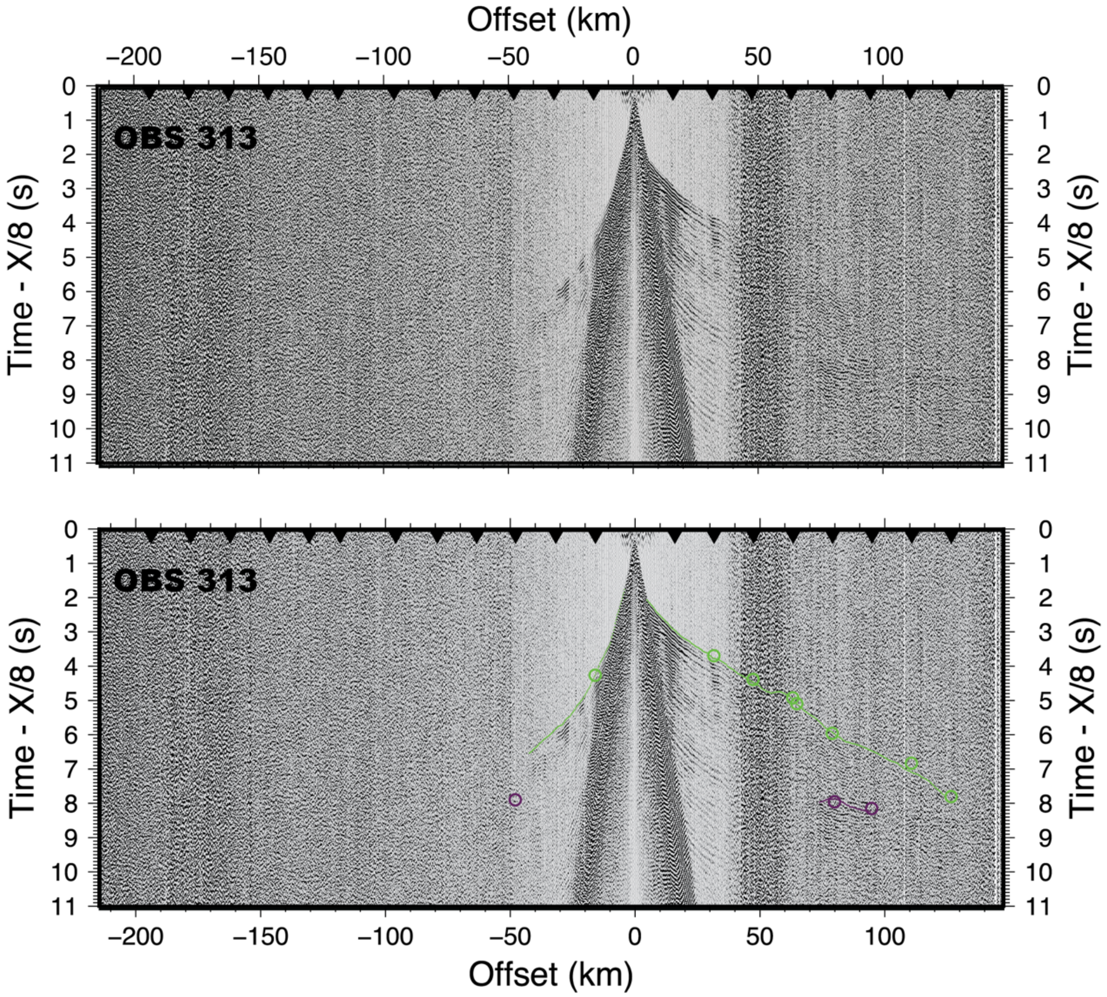

Figure A7: (Top panel) Processed seismogram for OBS 313, plotted with a reduction velocity of 8 km/s. (Bottom panel) Same seismogram with observed travel-time picks (small colored circles) and reciprocal travel-time picks from nearby OBS (large colored circles). See appendix text for color/seismic phase descriptions.

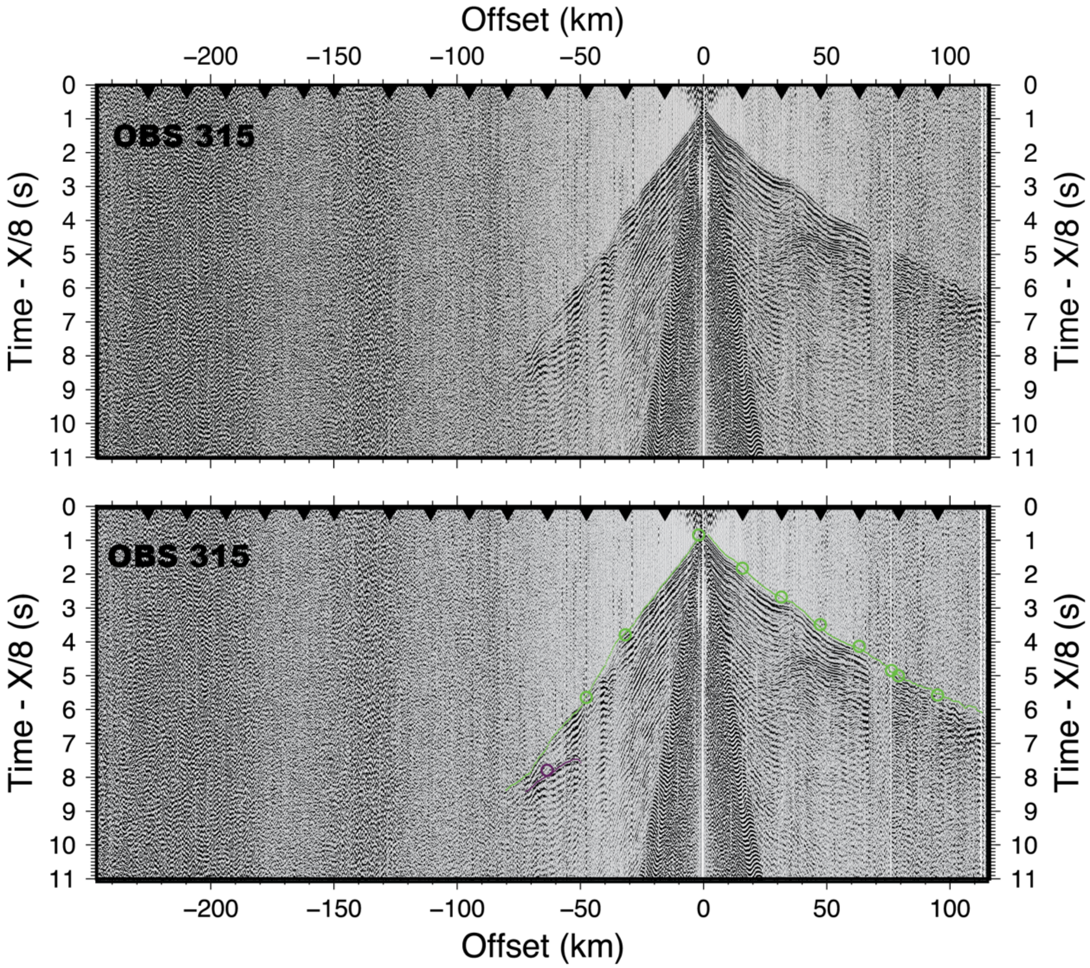

Figure A8: (Top panel) Processed seismogram for OBS 315, plotted with a reduction velocity of 8 km/s. (Bottom panel) Same seismogram with observed travel-time picks (small colored circles) and reciprocal travel-time picks from nearby OBS (large colored circles). See appendix text for color/seismic phase descriptions.

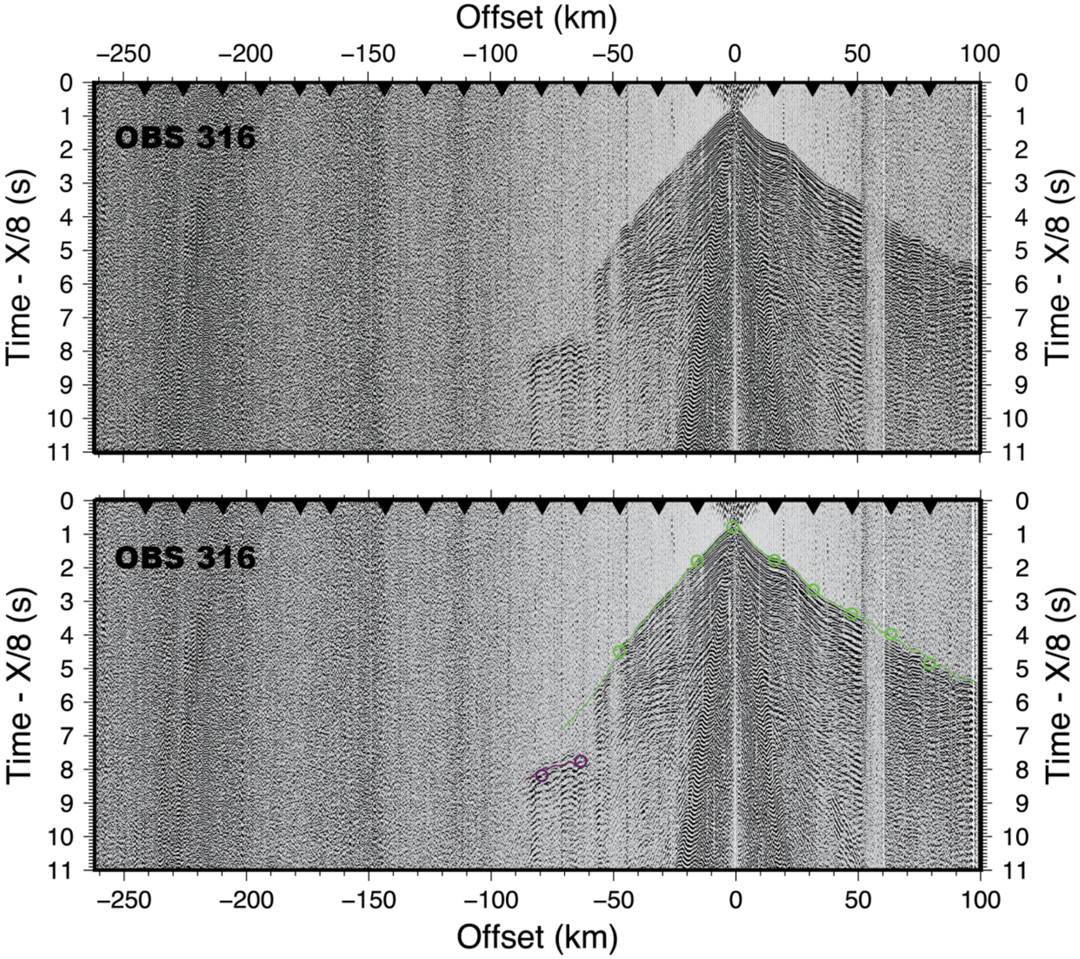

Figure A9: (Top panel) Processed seismogram for OBS 316, plotted with a reduction velocity of 8 km/s. (Bottom panel) Same seismogram with observed travel-time picks (small colored circles) and reciprocal travel-time picks from nearby OBS (large colored circles). See appendix text for color/seismic phase descriptions.

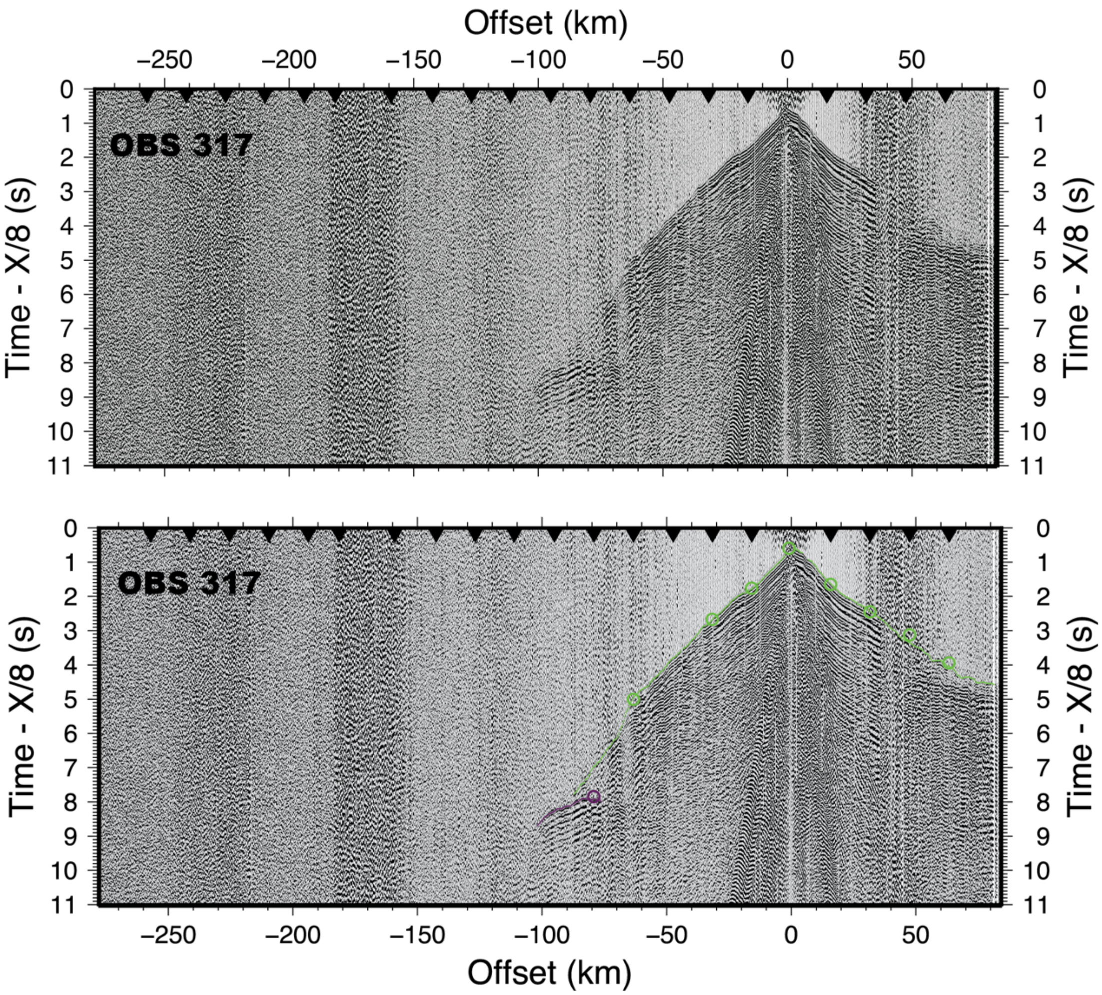

Figure A10: (Top panel) Processed seismogram for OBS 317, plotted with a reduction velocity of 8 km/s. (Bottom panel) Same seismogram with observed travel-time picks (small colored circles) and reciprocal travel-time picks from nearby OBS (large colored circles). See appendix text for color/seismic phase descriptions.

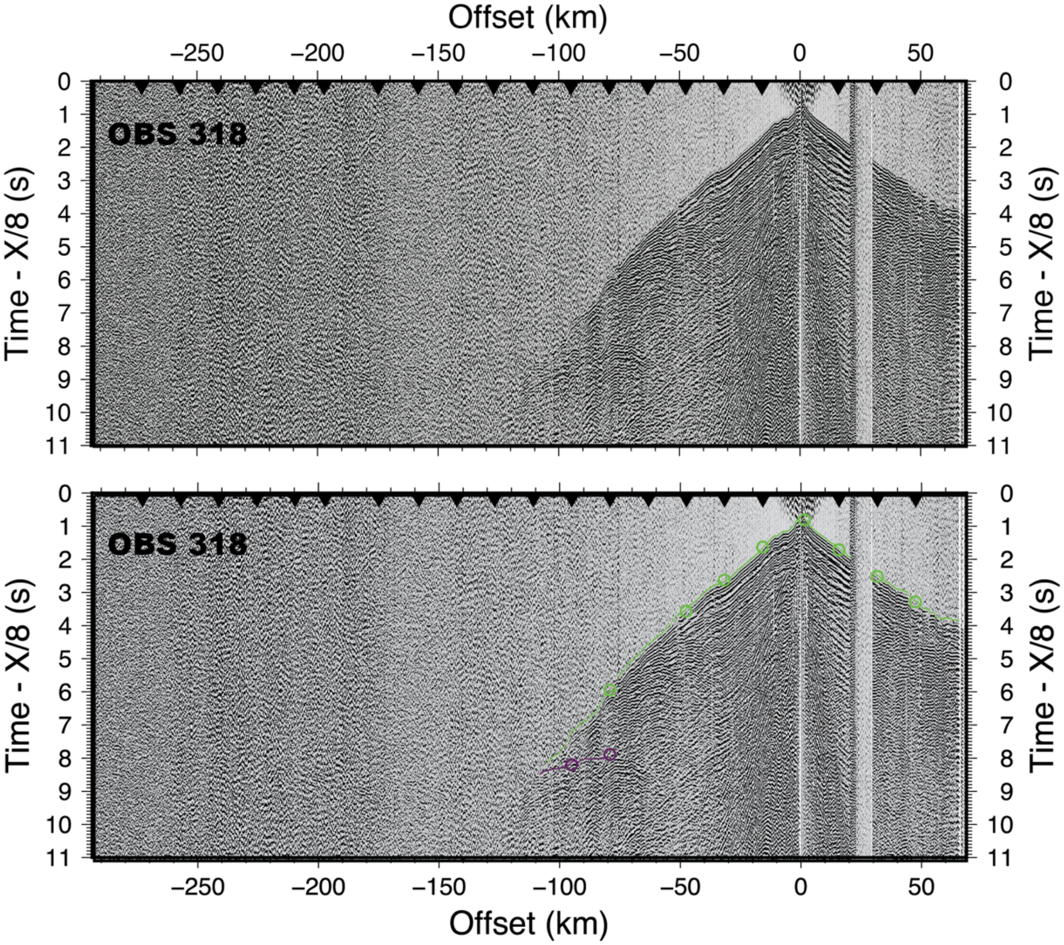

Figure A11: (Top panel) Processed seismogram for OBS 318, plotted with a reduction velocity of 8 km/s. (Bottom panel) Same seismogram with observed travel-time picks (small colored circles) and reciprocal travel-time picks from nearby OBS (large colored circles). See appendix text for color/seismic phase descriptions.

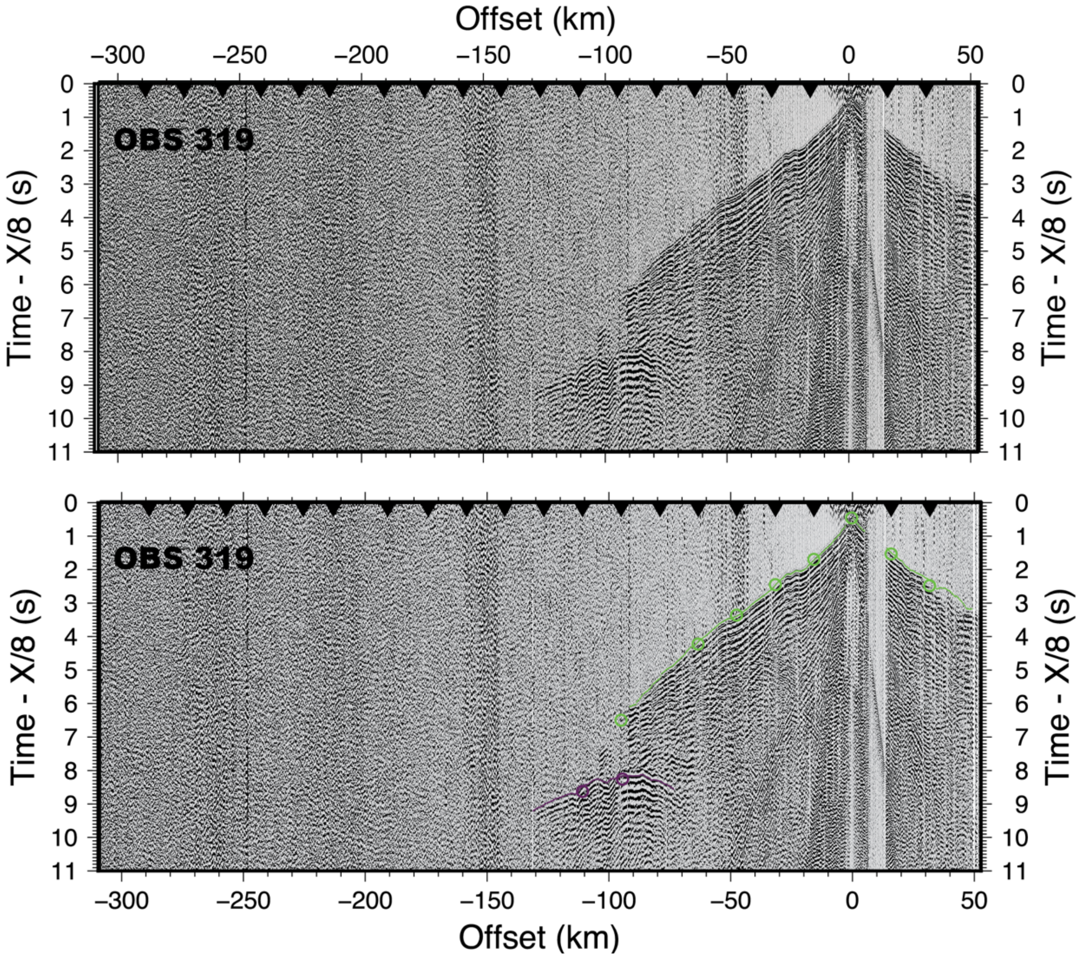

Figure A12: (Top panel) Processed seismogram for OBS 319, plotted with a reduction velocity of 8 km/s. (Bottom panel) Same seismogram with observed travel-time picks (small colored circles) and reciprocal travel-time picks from nearby OBS (large colored circles). See appendix text for color/seismic phase descriptions.

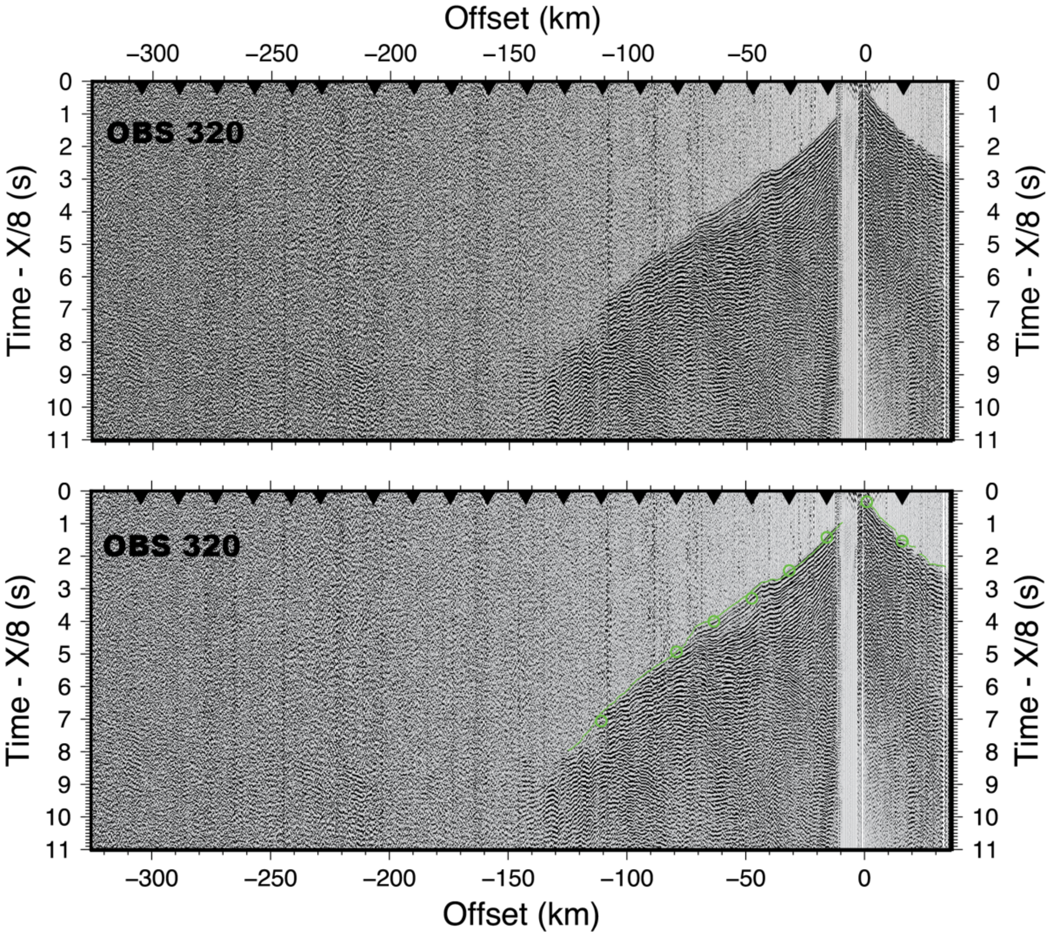

Figure A13: (Top panel) Processed seismogram for OBS 320, plotted with a reduction velocity of 8 km/s. (Bottom panel) Same seismogram with observed travel-time picks (small colored circles) and reciprocal travel-time picks from nearby OBS (large colored circles). See appendix text for color/seismic phase descriptions.

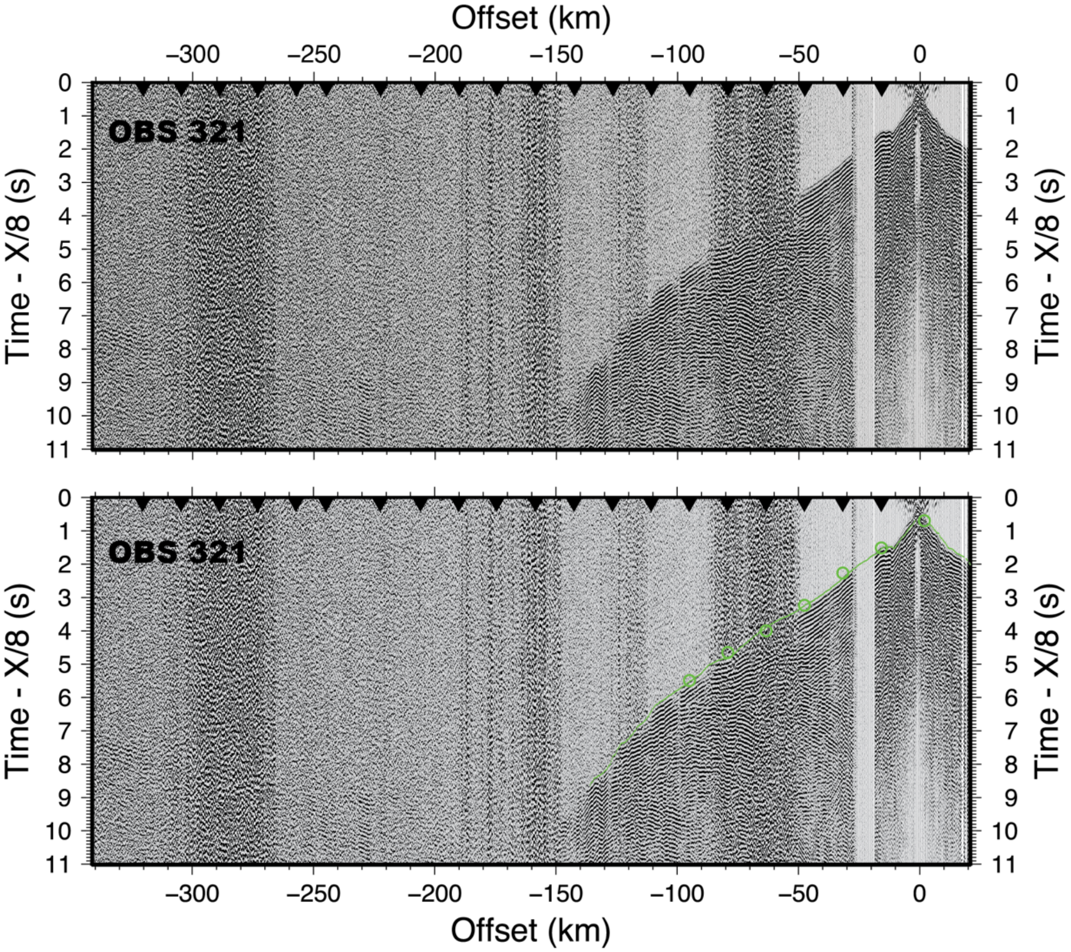

Figure A14: (Top panel) Processed seismogram for OBS 321, plotted with a reduction velocity of 8 km/s. (Bottom panel) Same seismogram with observed travel-time picks (small colored circles) and reciprocal travel-time picks from nearby OBS (large colored circles). See appendix text for color/seismic phase descriptions.